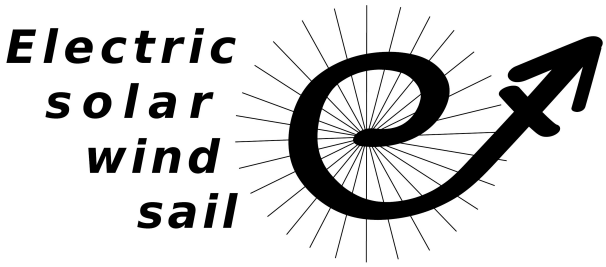

ESAIL D53.2
Refined design concepts document

Work Package: **WP 53**

Version: **Version 1.0**

Prepared by:	Finnish Meteorological Institute, Pekka Janhunen
Time:	Helsinki, Aug 30th, 2013
Coordinating person:	Pekka Janhunen, pekka.janhunen@fmi.fi

(List of participants:)

Participant no.	Participant organisation	Abbrev.	Country
1 (Coordinator)	Finnish Meteorological Institute	FMI	Finland

Table of Contents

1. Applicable documents

AD-1: Deliverable D52.1 “Conceptual E-sail designs and specifications for component development”
AD-2: Janhunen, P., A. Quarta and G. Mengali G., *Electric solar wind sail mass budget model,* Geosci. Instrum. Method. Data Syst., 2, 85-95, 2013 (**Appendix 1**)
AD-3: Deliverable D41.2 “Design description of the Remote Unit”
AD-4: Deliverable D41.3 “Test plan of the Remote Unit”
AD-5: Deliverable D41.4 “Remote Unit test results”
AD-6: Toivanen, P. and P. Janhunen, *Spin plane control and thrust vectoring of electric solar wind sail by tether potential modulation*, J. Prop. Power, 29, 178-185, 2013 (**Appendix 2**)
AD-7: Janhunen, P., *Photonic spin control for solar wind electric sail*, Acta Astronautica, 83, 85-90, 2013
AD-8: Deliverable D41.1 “Requirements specification of the Remote Unit”
AD-9: Janhunen, P., E*lectric sail, photonic sail and deorbiting applications of the freely guided photonic blade*, Acta Astronautica, in press, 2013

2. Introduction

In WP52 [AD1] different geometric E-sail models were analysed and one of them (the stretched auxiliary tether model) was selected for further development within the ESAIL project. The purpose of the present deliverable is to refine the chosen E-sail concept to take into account data from prototypes that are meanwhile developed in other WP2x-4x by developing models for mass and power budget and estimate the solar distance range where Remote Units remain functional.

3. Mass and power budgets

Mass and power budgets are detailed in the peer-reviewed paper [AD2] which is added to this document as Appendix 1. The paper adopts its Remote Unit parametres from the Remote Unit design [AD3]. In March 2013, the Remote Unit prototype which was built according to the design successfully passed environmental testing at DLR [AD4,AD5]. Thus the E-sail mass budget model which is given in [AD2] is supported by a functional Remote Unit prototype which underwent environmental testing.
Remote Unit propellant is needed in the tether rig deployment phase. If the mission orbits the sun (i.e., if the heliocentric phase angle of the spacecraft changes a lot during the E-sail propulsive phase of the mission), there is also a secular tendency of the spin rate to accelerate (decelerate) if the spacecraft spirals outward (inward) in the solar system [AD6]. This effect must then be compensated by Remote Unit propulsion. Formulas given in [AD6] allow one to predict the amount of Remote Unit delta-v and propellant needed for a given size of E-sail, E-sail inclination, orbit and mission duration. The mass budgets given in AD3 correspond to one possible scenario for the amount of propellant required. AD6 is added to this document as Appendix 2. In some types of missions this extra propellant consumption does not occur or is insignificant. This is the case for off-Lagrange point space weather monitoring (because although the E-sail orbits the sun for years, its

inclination angle with respect to the solar wind remains zero) and for fast mission out of the solar system (because the probe moves outward so rapidly that it does not revolve around the sun).
In this ESAIL project, two thruster options were considered and prototyped for the Remote Unit: cold gas thruster and FEEP thruster. We have also thought about using photonic blade thrusters instead [AD7]. Photonic blade thrusters would have the benefit of having infinite specific impulse so that the delta-v budget of the Remote Unit would no longer be a relevant parametre. For 20 km tethers, a 3-4 m² blade per Remote Unit is large enough to counteract the secular spinrate modification [AD7].

4. Remote Unit solar distance range

The tested Remote Unit prototype is designed for 0.9-4 au solar distance range, including maximum of 60º inclination with respect to sunlight [AD8]. This radial distance range was agreed upon in a project meeting before the Remote Unit design started. The adopted radial distance range covers all near-Earth missions, all asteroid main belt missions and missions where the E-sail acts as a booster stage for an outer solar system mission. For missions going to the inner solar system (Venus, Mercury or the near-Sun region), a “hot” version of our Remote Unit design could be generated by relatively minor modifications (for example, one which is suitable for ~0.25-1.1 au solar distance range). The mass of such “hot” Remote Unit version would likely not differ markedly from the prototyped case. It would be more challenging although not impossible to make a unit with extended radial distance range, i.e. one which works both in the near-sun region and in the outer realm of the asteroid belt, using the general Remote Unit concept used in WP4x.

5. Extra topic: auxtether-free E-sail model

We have also pursued a newer alternative E-sail geometric concept which does not include auxiliary tethers, but relies on actively “flying” each main tether actively by a sufficiently large tiltable photonic blade [AD9]. In this case the photonic blade must be larger than in the auxiliary tether case, because the photonic blade must produce enough thrust aligned in the spin plane to avoid mutual collisions between tethers. According to our simulations, ~20 m² blade for a 20 km long tether is enough for this purpose. If the solar wind has extremely strong variations, this blade area might be insufficient, but if that happens, it is always possible to avoid tether collisions by temporarily throttling back E-sail thrust by reducing the voltage of the electron gun.
The freely guided photonic blades (FGPBs) introduced in [AD9] could also be used for implementing a photonic heliogyro sail which has higher packing efficiency in stowed condition than a traditional heliogyro whose rectangular blades are actuated from the main spacecraft. A configuration which is similar to the FGPB-E-sail would also be possible to use in low Earth orbit (LEO) for deorbiting satellites by the electrostatic tether plasma brake effect; in that case the FGPBs would also augment their photonic thrust action by the upper atmosphere neutral drag. Analogously, the FGPB-heliogyro could be used for neutral drag based deorbiting. Finally, it is possible to envision hybrid heliogyro/E-sail where e.g. the heliogyro works when the probe is inside the magnetosphere and the more efficient E-

sail takes over when the probe is in a region where solar wind exists.

6. Conclusion

A detailed auxtether-based E-sail concept has been developed whose quantitative mass and power budget was published as a peer-reviewed article [AD2]. The model is based on parametres of the constructed Remote Unit prototype which underwent and passed environmental testing. A quantitative way to predict the Remote Unit propellant consumption and thus to size its tanks was developed and published in another peer-reviewed article [AD6]. Photonic blade concepts (with or without auxiliary tethers) which provide infinite specific impulse and thus avoid Remote Unit propellant tank sizing issues were also developed and published as two additional peer-reviewed articles [AD7, AD9].

We conclude that a large-scale high performance E-sail has been successfully pushed to TRL 4 and partly to TRL 5. Depending on the mission, the developed model may have some Remote Unit propellant capacity issues because of the secular change of the spin rate. To resolve these potential issues, propellantless photonic blade concepts were therefore also developed at lower TRL. As an alternative, “advanced” E-sail technology, auxtether-free FGPB variants were developed as well at low TRL. The FGPB variants provide potential benefits especially in terms of better modularity.

APPENDIX 1 [AD2]

Janhunen, P., A. Quarta and G. Mengali, “*Electric solar wind sail mass budget model*”, Geosci. Instrum. Method. Data Syst., 2, 85-95, 2013

Geosci. Instrum. Method. Data Syst., 2, 85–95, 2013
www.geosci-instrum-method-data-syst.net/2/85/2013/
doi:10.5194/gi-2-85-2013

Geoscientific Instrumentation Methods and Data Systems
Open Access

Electric solar wind sail mass budget model

P. Janhunen[1], **A. A. Quarta**[2], **and G. Mengali**[2]

[1]Finnish Meteorological Institute, Helsinki, Finland
[2]Department of Civil and Industrial Engineering, University of Pisa, Pisa, Italy

Correspondence to: P. Janhunen (pekka.janhunen@fmi.fi)

Received: 24 May 2012 – Published in Geosci. Instrum. Method. Data Syst. Discuss.: 10 July 2012
Revised: 12 November 2012 – Accepted: 28 January 2013 – Published: 19 February 2013

Abstract. The electric solar wind sail (E-sail) is a new type of propellantless propulsion system for Solar System transportation, which uses the natural solar wind to produce spacecraft propulsion. The E-sail consists of thin centrifugally stretched tethers that are kept charged by an onboard electron gun and, as such, experience Coulomb drag through the high-speed solar wind plasma stream. This paper discusses a mass breakdown and a performance model for an E-sail spacecraft that hosts a mission-specific payload of prescribed mass. In particular, the model is able to estimate the total spacecraft mass and its propulsive acceleration as a function of various design parameters such as the number of tethers and their length. A number of subsystem masses are calculated assuming existing or near-term E-sail technology. In light of the obtained performance estimates, an E-sail represents a promising propulsion system for a variety of transportation needs in the Solar System.

1 Introduction

The electric solar wind sail (E-sail) is an innovative deep space propulsion concept that uses the solar wind dynamic pressure for generating thrust without the need of reaction mass (Janhunen, 2006, 2009; Janhunen et al., 2010). The E-sail spacecraft is spun around its symmetry axis and uses the centrifugal force to deploy and stretch out a number of thin, long and conducting tethers, which are kept in a high positive potential by an onboard electron gun pumping out the negative charge from the system (Janhunen et al., 2010). The latter compensates the electron current gathered by the conducting tethers from the surrounding solar wind plasma. The charged tethers experience Coulomb drag with the high-speed solar wind plasma stream and, thus, generate a propulsive thrust that is mechanically transmitted to the spacecraft by a slight bending of the tethers perpendicular to their spin plane (Fig. 1).

Our reference full-scale E-sail propulsion system comprises 2000 km of total main tether length (for example 100 tethers, each one being 20 km long), with 25 kV tether voltage, 960 W electron gun power consumption and 1.16 N nominal thrust at 1 AU from the Sun (Janhunen et al., 2010). If the main tethers are sufficiently long such that the electric potential structure overlapping between them is negligible, the propulsive thrust varies as $1/r$, where r is the Sun–spacecraft distance (Janhunen, 2009). Note, for comparison, that in the classical photonic solar sail (Wright, 1992; McInnes, 1999) the propulsive thrust decreases more rapidly (that is, as $1/r^2$) with the solar distance. Therefore the E-sail concept is especially attractive for a mission towards the outer Solar System, such as a Jupiter rendezvous (Quarta et al., 2011) or a mission towards the heliopause (Quarta and Mengali, 2010) and the Solar System boundaries.

The previous assertion about the overlapping negligibility between electric potential structures of different tethers can be justified as follows. At 1 AU the potential structure radius is ~ 100 m under average solar wind conditions (Janhunen, 2009). In all E-sail models considered in this paper the distance between the tether tips is $2\pi \times 20$ km$/100 =$ 1257 m. Thus, under usual conditions, overlapping affects about 200 m$/1257$ m $= 16$ % of the tether length. The electric potential structures scale as proportional to the solar distance r because they are proportional to the plasma Debye length which goes as $\sim 1/\sqrt{n}$, where n is the plasma density and $n \sim 1/r^2$. Therefore, at 4 AU the overlapping can affect ~ 64 % of the tether length. Near the main spacecraft, where the tethers are close one to the other, they form an effectively impenetrable obstacle to solar wind ions such that ions are

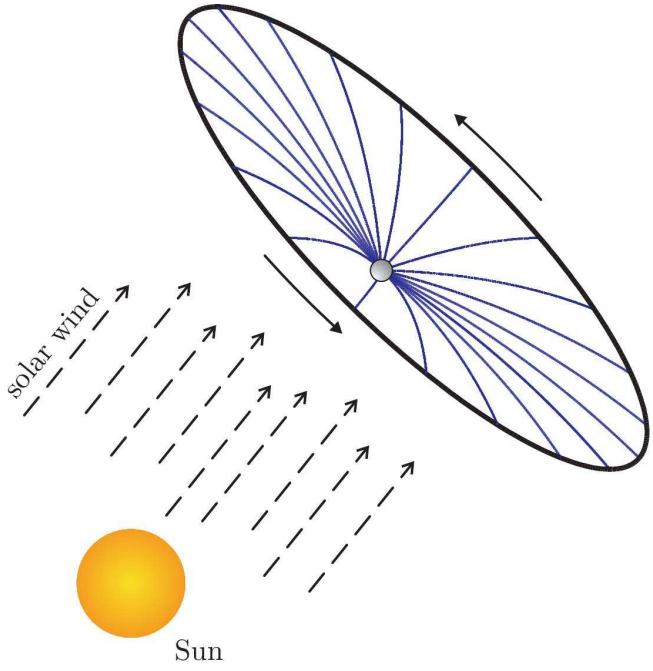

Fig. 1. Schematic view of a spinning E-sail.

reflected back. A model of how the thrust behaves inside the overlap region is not yet available. We roughly estimate that on average, within the overlapping region, the thrust is 60 % of the free tether value. This implies that at 1 AU the thrust would be reduced by ~ 6 % by the overlapping effect and at 4 AU the reduction would be ~ 25 %.

The E-sail propulsive thrust per unit length (of a main tether) is about $580\,\mathrm{nN\,m^{-1}}$ so that, for example, a 20 km long tether gathers about 11.6 mN of thrust from the surrounding solar wind plasma (Janhunen et al., 2010). The previous thrust estimate at 1 AU corresponds to an average solar wind. Actually, the solar wind properties vary widely along, basically, all relevant timescales. However, due to certain plasma physical effects such as Debye length scaling, the E-sail propulsive thrust tends to vary much less than the solar wind dynamic pressure when a simple constant power strategy is applied to adjust the tether voltage in response to solar wind density variations (Toivanen and Janhunen, 2009).

The spacecraft, with its attached main tethers, is spun so that the centrifugal force overcomes the propulsive thrust by a factor of about 5. Accordingly, each main tether has to withstand about 5 cN (cN = centinewton = about 1 gram's weight in Earth's gravity) continuous pull force without breaking. In addition, the main tethers must survive the micrometeoroid impacts over the mission's lifetime (Hoyt and Forward, 2000), whose maximum reference value is about ten years. These requirements are filled with sufficient margin by a four-line Heytether (Seppänen et al., 2011), produced by ultrasonic bonding from 25 µm and 50 µm aluminium wires (Kurppa et al., 2010). A Heytether consists of one parallel wire to which several (by default 3) loop wires are bonded to the base wire at regular, mutually interleaving intervals. In terms of micrometeoroid tolerance, the four-wire Heytether is roughly equivalent to the criss-crossed four-wire Hoytether (Hoyt and Forward, 2000), but is easier to manufacture by our methods because only one base wire is needed.

Assuming ten years of flight time with full thrust of 1 N at about 1 AU, an E-sail propulsion system produces a total impulse of about 300 MNs. This value is equivalent to the total impulse produced by a high-thrust propulsion system, for example, a chemical rocket with a specific impulse of 300 s burning 100 tonnes (t) of propellant, or an electric thruster with a specific impulse of 3000 s that uses 10 t of propellant.

The propulsive acceleration and the corresponding mission performance in terms of flight time depend on both the payload mass and the E-sail design parameters. In order to evaluate the actual E-sail capabilities in a deep-space next generation mission, it is therefore important to have a parametric model that is able to model the propulsion system performance as a function of its (main) design parameters. The purpose of this paper is to develop such a parametric model. The new mathematical model deepens and updates the previous simplified approach of Mengali et al. (2008).

The fact that the E-sail spins slowly has some implications for the payload, especially to imaging science instruments requiring a combination of accurate pointing and lengthy exposure. Specific technical solutions such as despun platforms are available to mitigate or eliminate these potential issues. Analyzing such matters is outside the scope of this paper.

2 Scalable E-sail mathematical model

We now consider a parametric model for mass budgeting of E-sail missions of different sizes, see e.g. Larson and Wertz (1999) for the general approach. Consider an E-sail propulsion system, consisting of a main body and N main tethers, each one with length L. A remote unit (RU) is placed at the tip of each tether, see Fig. 2. Every RU comprises two reels for deploying an auxiliary tether, as discussed next, and a thruster unit for controlling the main tether's angular velocity. The main spacecraft and the tether rig spin slowly to keep the tethers taut, a typical spin period being some tens of minutes. The reason for including the auxiliary tethers is that they keep the tether rig dynamically stable without the need of active control (Janhunen et al., 2010). The motivation for including RUs is to host the auxiliary tether reels and small thruster, whose purpose is to generate the initial angular momentum and possibly to control the spin rate later during flight, if needed.

The total spacecraft mass can be thought of as being the sum of the following contributions: (1) mission-specific payload of mass m_{pay}; (2) high voltage subsystem including electron guns; (3) N main tethers of mass m_{mt}, N main tether reels of mass m_{mr}, and N RUs of mass m_{ru}; (4) auxiliary

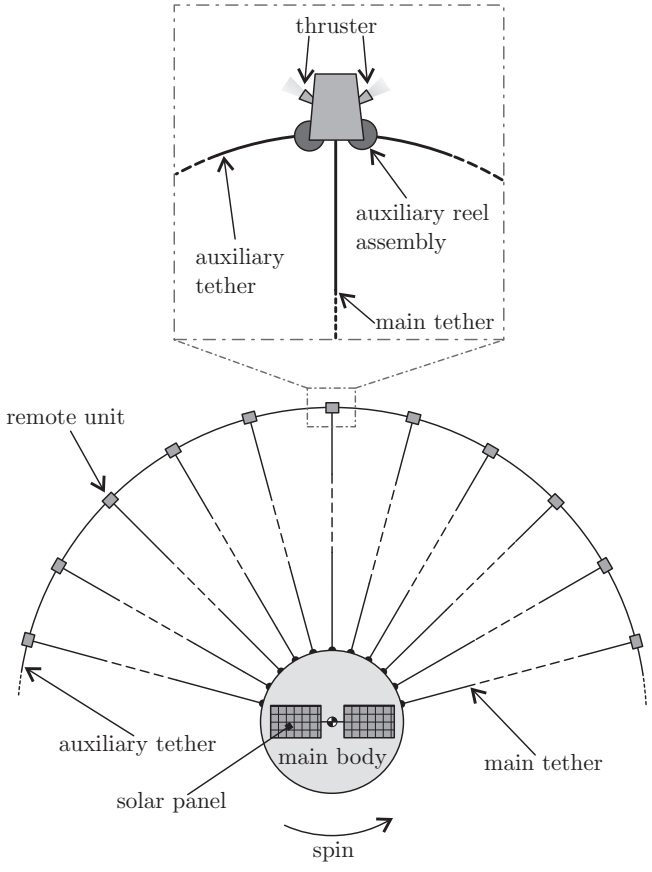

Fig. 2. Schematic view of E-sail with remote unit and auxiliary tethers.

tether of mass $m_{\rm at}$; (5) tether cameras and E-sail controller; (6) power system with solar panels; (7) telemetry system with antennas; (8) thermal control subsystem; (9) attitude control system (ACS); and (10) structural mass. The simplified expression for the total spacecraft mass m is thus

$$m = \eta_{\rm ma}\,\frac{m_{\rm b} + N\,(m_{\rm mt} + m_{\rm ru}) + m_{\rm at}}{(1-\eta_{\rm str})(1-\eta_{\rm acs})} \tag{1}$$

where the dimensionless margin coefficient $\eta_{\rm ma} = 1.2$ is introduced to account for a 20 % margin on the actual value, while $\eta_{\rm str}$ and $\eta_{\rm acs}$ model the structural mass fraction and the ACS mass fraction of the spacecraft's total mass.

Each term in the numerator of the right hand side of Eq. (1) can be expressed as a function of the system's parameters, as will be discussed below. The term $m_{\rm b}$ indicates the mass of the functional components of the main body of the spacecraft, given by

$$m_{\rm b} = \frac{m_{\rm gc} + m_{\rm vs} + n_{\rm ca}\,m_{\rm ca} + n_{\rm eg}\,m_{\rm eg} + m_{\rm sa} + \dfrac{m_{\rm pay}}{1-\eta_{\rm tms}} + N m_{\rm mr}}{1-\eta_{\rm tcs}}. \tag{2}$$

The mass of the high voltage source ($m_{\rm vs}$), guidance computer ($m_{\rm gc}$), tether cameras ($n_{\rm ca}\cdot m_{\rm ca}$), electron guns ($n_{eg}\cdot m_{\rm eg}$), solar array power system ($m_{\rm sa}$), the telemetry system equipped payload ($m_{\rm pay}/(1-\eta_{\rm tms})$) and the main tether reels ($N\cdot m_{\rm mr}$) are discussed in the following subsections, along with the other mass terms appearing in Eq. (1).

Note that the term "payload" in this paper refers to the payload instruments and the telemetry system, but it does not include the power system, structure or thermal control subsystems. The rationale for lumping the telemetry system with the payload is that the payload drives telemetry requirements, not the E-sail. On the other hand, the power system is kept separate because, typically, the payload uses only little power during the cruise phase and thus it makes sense to share the power system hardware between the E-sail and the payload.

2.1 High voltage subsystem

We assume $n_{\rm eg} = 3$ redundant electron guns, each one providing a beam power $P_{\rm eg}$ and having mass $m_{\rm eg} = \gamma_{\rm eg}\,P_{\rm eg}$, where the gun specific mass is $\gamma_{\rm eg} = 1.0\,{\rm kg\,kW^{-1}}$ (Zavyalov et al., 2006). We assume 100 % gun efficiency and neglect the low voltage cathode heating power. The electric power $P_{\rm eg}$ varies with the distance r from the Sun and can be related to the total length NL of the main tethers through a linear power density β, whose value essentially depends (Mengali et al., 2008) on the main tethers voltage and on the Heytether (Seppänen et al., 2011) total surface area. In particular, using the current Heytether configuration, the expression for the linear power density is

$$\beta = 2\,n_{\oplus}\sqrt{\frac{2e^3\,V_0^3}{m_e}}\,[R_1 + (3\pi/2)\,R_2], \tag{3}$$

where V_0 is the nominal voltage of the main tethers, $n_{\oplus} = 7.6\times10^6$ m^{-3} is the nominal solar wind density at $r = r_{\oplus} \equiv 1$ AU, e is the electron charge, and m_e is the electron mass. For example, assuming $V_0 = 25$ kV and the previous tether dimensions ($R_1 = 25\,\mu$m and $R_2 = 12.5\,\mu$m), Eq. (3) provides a linear power density $\beta \simeq 0.4790\,{\rm W\,km^{-1}}$.

Taking into account a reference condition that corresponds to the minimum Sun–spacecraft distance $r_{\rm min} = 0.9$ AU, a conservative estimate of the electric power required by the electron gun is

$$P_{\rm eg} = N\,L\,\beta\,(r_{\oplus}/r_{\rm min})^2\,. \tag{4}$$

Even though the solar wind density n exhibits large natural variations, a simple strategy of varying the tether voltage V away from the nominal V_0, such that $P_{\rm eg}$ is constant, is quite effective for maintaining constant the daily, weekly or monthly averaged thrust at a given solar distance r (Toivanen and Janhunen, 2009).

Two plasma physical effects are responsible for this, at first, surprising behavior. The first one is that the thrust is proportional to the total tether length times the tether's electron

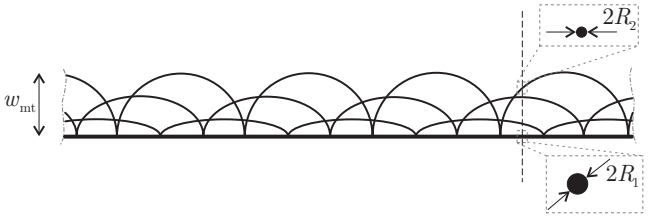

Fig. 3. Four-wire Heytether scheme.

sheath width. For a fixed voltage, the latter is proportional to the solar wind plasma Debye length, which, in turn, is proportional to $1/\sqrt{n}$. As a result (Janhunen, 2009), the thrust is approximately linearly proportional to the tether voltage V, but it has only a square root dependence on the solar wind dynamic pressure $P_{\rm dyn} = m_p n v^2$, where v is the solar wind speed and m_p is the proton mass. The second effect is that, because the tether current is proportional to $n\sqrt{V}$, V must be varied as $n^{-2/3}$ in order to maintain $P_{\rm eg}$ constant. When combined, these two effects imply that under a constant $P_{\rm eg}$ strategy the thrust is proportional to $n^{1/6}v$, i.e. the thrust depends only weakly on the solar wind density. Furthermore, solar wind variations of n and v are typically anticorrelated, and this tends to further reduce the thrust fluctuations.

There are several methods on how high voltage distribution (and grounding plan) can be obtained. One way is to have a relatively low energy (e.g. 1 kV) electron gun connected to a common internal bus that maintains the electron gun at its voltage. Each tether can then have its own small, high voltage source, thus allowing an arbitrary differential modulation of tether voltages and no need for high voltage switches, resistors, potentiometers or cables. The high voltage source mass is assumed to be $m_{\rm vs} = \gamma_{\rm vs} P_{\rm eg}$, where $\gamma_{\rm vs} = 20\,{\rm kg\,kW^{-1}}$ is the specific mass of the high voltage generator. For example, Ultravolt (http://www.ultravolt.com) makes $30\,{\rm W\,kV^{-1}}$ vacuum compatible DC voltage source model 35A24-P30 with a $\gamma_{\rm vs}$ of $14.2\,{\rm kg\,kW^{-1}}$ and an efficiency of 70 %. Therefore a value of $20\,{\rm kg\,kW^{-1}}$ seems to be a reasonable value, even though it may require some customization effort. As for the space qualified high voltage systems, electron guns with up to 40 kV accelerating voltage have been successfully operated on sounding rockets for scientific purposes (Nemzek and Winckler, 1991).

2.2 Main tethers

The main tether is a four-wire aluminium (density $\rho_{\rm Al} = 2700\,{\rm kg\,m^{-3}}$) Heytether (Seppänen et al., 2011), composed of a (straight) base wire of radius $R_1 = 25\,\mu{\rm m}$, and three (approximately semicircular) loop wires of radius $R_2 = 12.5\,\mu{\rm m}$, the latter being ultrasonically bonded to the former (Kurppa et al., 2010), see Fig. 3.

The mass per unit length of the main tether is $\lambda_{\rm mt} = \rho_{\rm Al}\pi\left[R_1^2 + (3\pi/2)\,R_2^2\right] \simeq 1.155 \times 10^{-5}\,{\rm kg\,m^{-1}}$. Therefore, the tether mass $m_{\rm mt}$ depends linearly on L according to the simple relationship

$$m_{\rm mt} = \lambda_{\rm mt}\, L. \tag{5}$$

2.3 Main tether reel assembly

The main tether reel assembly is a motorized mechanism that holds the reeled tether inside, and deploys it in orbit. Its mass is estimated to be

$$m_{\rm mr} = m_{\rm mr0} + \rho_{\rm mr}\,\frac{V_{\rm mt}}{\eta_{\rm mr}}, \tag{6}$$

where $m_{\rm mr0} = 0.1$ kg corresponds to the mass of the motorized reel assembly in case of a short tether such as that used in ESTCube-1 (Janhunen et al., 2010; Pajusalu et al., 2012) and Aalto-1 (Praks et al., 2011; Näsilä et al., 2011) CubeSat missions, $\rho_{\rm mr} = 500\,{\rm kg\,m^{-3}}$ is the assumed mass density of the reel structure with respect to its contained volume, $V_{\rm mt} = m_{\rm mt}/\rho_{\rm Al}$ is the solid aluminium volume of the main tether and $\eta_{\rm mr} = 0.3$ is the packaging factor of the reeled tether.

2.4 Auxiliary tether

The auxiliary tether is manufactured using Kapton (with a density $\rho_{\rm Ka} = 1420\,{\rm kg\,m^{-3}}$) and is used to connect the RUs for avoiding collisions between adjacent tethers (Janhunen et al., 2010). Assuming that the auxiliary tether is constituted by a rectangular section of height $h_{\rm at} = 12.7\,\mu{\rm m}$ and width $w_{\rm at} = 3$ cm, its linear density is $\lambda_{\rm at} = \eta_p\,\rho_{\rm Ka}\,h_{\rm at}\,w_{\rm at} = 2.705 \times 10^{-4}\,{\rm kg\,m^{-1}}$ where $\eta_{\rm p} = 0.5$ is a dimensionless coefficient that models the perforation of the auxiliary tether's stripe required to produce a proper amount of elasticity. The length of the auxiliary tether is approximately equal to the length of a circumference of radius L. The total auxiliary tether mass is thus

$$m_{\rm at} = \lambda_{\rm at}\, 2\pi\, L. \tag{7}$$

2.5 Remote units

Each RU hosts a thruster for initiating and (possibly later) controlling the tether rig's spin. It also includes the reels from which the auxiliary tethers are deployed. Two thruster options are being considered in more detail, a cold gas thruster of Nanospace and an ionic liquid FEEP (Field Emission Electric Propulsion) thruster of Alta (Marcuccio et al., 2011). The cold gas thruster can produce a total impulse sufficient for the required initial spin and for the small spin rate adjustments during flight operations. The FEEP thruster, on the other hand, has a total impulse capability sufficient for controlling the spin to counteract the Coriolis acceleration that results from orbiting around the Sun with an inclined sail (Toivanen and Janhunen, 2012).

Prototypes of cold gas thruster and FEEP thruster equipped RUs have been designed at Ångström Space Technology Centre (Wagner et al., 2012). The wet mass of a

FEEP-unit is 0.880 kg, whose auxiliary tether reel system's share is 0.135 kg. The mass of the ionic liquid propellant is 0.07 kg and the total impulse capability 2000 Ns. The wet mass of a cold-gas unit is 0.613 kg, of which 0.05 kg is propellant, and the total impulse capability is 40 Ns.

For conservative purposes, here we assume that each RU contains a FEEP thruster that is mounted either along the spin accelerating direction or along the decelerating direction, see Fig. 2. Therefore there are two subtypes of RUs, which are otherwise identical except being mirror images of each other in the left–right direction. In a baseline configuration, accelerating and braking thrusters are alternated on adjacent RUs. More general arrangements could also be considered in specific missions. Accordingly, the RU's mass with a FEEP unit is parameterized as

$$m_{\rm ru} = m_{\rm ru0} + \frac{m_{\rm at}}{\rho_{\rm Ka}}\,\rho_{\rm ar}\ , \tag{8}$$

where $m_{\rm ru0} = 0.745$ kg and $\rho_{\rm ar} = 282\,{\rm kg\,m^{-3}}$.

2.6 Tether cameras and controller

To find out the actual position of each RU at the main tether tips, a number $n_{\rm ca} = 12$ of cameras along the perimeter of the main spacecraft are used. Each camera has a mass of $m_{\rm ca} = 0.04$ kg (Pappa et al, 2004). Each RU has an optical beacon transmitting a unique optical coding so that the unit can be identified by the cameras. The E-sail also needs a guidance computer to which a mass $m_{\rm gc} = 1$ kg is allocated, including the radiation shielding. Since the tether rig moves slowly, a moderate amount of computing power is sufficient.

2.7 Power generation subsystem

The power generation subsystem includes solar panels with their deployment mechanism as well as a power processing unit that produces bus voltage and, very likely, a battery pack.

For a baseline deep space mission, where the Sun-spacecraft distance ranges between about 0.9 AU and 4 AU, rather large solar panels are typically needed to provide the payload with a sufficient power up to the aphelion radius. It is assumed that during the cruise phase both payload and telemetry instruments are in idle (or keep-alive) mode, with a specific power consumption of $0.1\,{\rm W\,kg^{-1}}$, while during the operating mode (that is, when the E-sail is turned off) the power consumption is $1\,{\rm W\,kg^{-1}}$. To be conservative, we assume that the E-sail could also use 10 W of base power in addition to the electron gun requirement, even when it is turned off. Note that the electric power required by the electron gun varies with the solar distance as $1/r^2$, that is, in the same way as the illumination of the solar panels.

For sizing the payload, it turns out that the power system requirements are always driven by the payload requirements at 4 AU (aphelion distance), and not by the E-sail requirements during the cruise phase. Hence, the power system has to provide $1\,{\rm W\,kg^{-1}}$ for the payload and telemetry units at 4 AU, plus 10 W of base power for the E-sail. Note that at closer solar distances the power system produces more power than is actually necessary. We assume a specific mass value of $\gamma_{\rm sa} = 10\,{\rm kg\,kW^{-1}}$ for the power subsystem as a whole, when the reference kW-value is the full power gathered at 0.9 AU. This is motivated by the fact that the full panel power at 0.9 AU does not need to be processed by the power processing unit. It has only to provide enough power to the payloads and to guarantee the solar panels health. We also assume an end-of-life solar panel degradation factor of $\eta_{\rm sa} = 1.2$: where power produced by the panels at end-of-life is assumed to be $\eta_{\rm sa}$ times less than at beginning of life.

Accordingly, the power produced by the solar arrays at the maximum distance $r_{\rm max} = 4$ AU is

$$P_{\rm sa}^{\rm rmax} = \eta_{\rm sa}\left[P_{\rm o} + \max\left(\eta_{\rm vs}P_{\rm eg}\left(\frac{r_{\rm min}}{r_{\rm max}}\right)^2 + \eta_{\rm ka}P_{\rm pay},\, P_{\rm pay}\right)\right], \tag{9}$$

where $P_{\rm pay} = m_{\rm pay}/\gamma_{\rm pay}$ is the payload required power, $\eta_{\rm ka} = 0.1$ is the idle versus duty power ratio of both the payload and the telemetry systems, and $\eta_{\rm vs} = 1.25$ is the assumed overhead factor (reciprocal of the efficiency) of the HV source. Correspondingly, the needed solar array power at the minimum distance $r_{\rm min} = 0.9$ AU is

$$P_{\rm sa}^{\rm rmin} = \eta_{\rm sa}\left[P_{\rm o} + \max\left(\eta_{\rm vs}P_{\rm eg} + \eta_{\rm ka}P_{\rm pay},\, P_{\rm pay}\right)\right]. \tag{10}$$

From the $1/r^2$ scaling of the solar radiation flux, it follows that the needed maximum capacity of the solar arrays scaled to $r_{\rm min}$ is

$$P_{\rm sa} = \max\left[P_{\rm sa}^{\rm rmin},\, P_{\rm sa}^{\rm rmax}\,(r_{\rm max}/r_{\rm min})^2\right]. \tag{11}$$

Finally, the mass of the power subsystem is given by $m_{\rm sa} = \gamma_{\rm sa}P_{\rm sa}$. Recall that an underlying assumption in the above formulas is that the science payload is active during coasting phases and dormant during propulsive phases, the dormant payload power being factor $\eta_{\rm ka}$ times the active payload power.

2.8 Telemetry, ACS, thermal and structure

We assume that the telemetry subsystem mass is related to the payload such that the telemetry subsystem plus payload mass is given by $m_{\rm pay}/(1-\eta_{\rm tms})$, where the telemetry mass fraction is $\eta_{\rm tms} = 0.2$. This choice is qualitatively motivated by the fact that each scientific instrument included in the payload usually generates data that must be transmitted by the telemetry system. If a payload needs more telemetry capability than is assumed here, one has to reserve extra mass for it from the payload budget. Our results concerning the E-sail mass fraction are not sensitive to the previous parametric choice.

The E-sail requires a service from the satellite's attitude control system (ACS) for pointing the spin axis towards the

Table 1. Physical reference data.

Parameter	Symbol	Value
Thrust/length/voltage	f_0	24.2 nN/(kV m)
Nominal tether voltage	V_0	25 kV
Thrust per length	f_V	24.2 nN m^{-1}
Aux. tether thickness	$h_{\rm at}$	12.7 µm
Main reel base mass	$m_{\rm mr0}$	0.1 kg
Tether camera mass	$m_{\rm ca}$	0.04 kg
Number of tether cameras	$n_{\rm ca}$	12
E-sail computer mass	$m_{\rm gc}$	1 kg
FEEP Remote Unit base m.	$m_{\rm ru0}$	0.745 kg
Number of electron guns	$n_{\rm eg}$	3
1 AU solar wind density	$n_\oplus$	7.6 cm^{-3}
E-sail base power	$P_{\rm o}$	10 W
Heytether base wire radius	R_1	25 µm
Heytether loop wire radius	R_2	12.5 µm
Minimum solar distance	$r_{\rm min}$	0.9 AU
Maximum solar distance	$r_{\rm max}$	4.0 AU
Aux. tether width	$w_{\rm at}$	3 cm
Telemetry mass fraction	$\eta_{\rm tms}$	0.2
ACS mass fraction	$\eta_{\rm acs}$	0.05
Overall mass margin factor	$\eta_{\rm ma}$	1.2
Main tether reel fill factor	$\eta_{\rm mr}$	0.3
Aux. tether perforation	$\eta_{\rm p}$	0.5
Solar panel EOL degrad. fac.	$\eta_{\rm sa}$	1.2
Structural fraction	$\eta_{\rm str}$	0.15
Therm. sys. mass fraction	$\eta_{\rm tcs}$	0.05
HV source loss factor	$\eta_{\rm vs}$	1.25
Payload mass per power	$\gamma_{\rm pay}$	1000 kg kW^{-1}
E-gun mass per power	$\gamma_{\rm eg}$	1 kg kW^{-1}
Power system mass per power	$\gamma_{\rm sa}$	10 kg kW^{-1}
HV source mass per power	$\gamma_{\rm vs}$	20 kg kW^{-1}
Aluminium density	$\rho_{\rm Al}$	2700 kg m^{-3}
Kapton density	$\rho_{\rm Ka}$	1420 kg m^{-3}
Aux. tether reel "density"	$\rho_{\rm ar}$	282 kg m^{-3}
Main reel "density"	$\rho_{\rm mr}$	500 kg m^{-3}

Sun and starting the spin motion at the beginning of E-sail deployment. Most of the required angular momentum is obtained from RU thrusters, but a small fraction is gotten from the ACS. If the mission calls for accurate manoeuvring near an asteroid or another small body, a micropropulsion system is needed for overcoming a small photonic sail effect of the tethers and for fine orbit control. We assume that the attitude and orbit control system (AOCS) mass is a fraction $\eta_{\rm acs} = 0.05$ of the spacecraft's total mass.

Similarly, the thermal control subsystem mass $m_{\rm tcs}$ is expressed as a given percentage of the main body mass through the coefficient $\eta_{\rm tcs} = 0.05$. Finally, the structural parts of the main spacecraft including RU launch locks is, by assumption, a fraction $\eta_{\rm str} = 0.15$ of the total mass. The main spacecraft parameters of the mass model are collected in Table 1.

Table 2. Spacecraft mass budget and some other properties for a characteristic acceleration $a_\oplus = 0.1\,{\rm mm\,s^{-2}}$.

Payload $m_{\rm pay}$ (kg)	100	200	500	1000
Number of tethers N	12	16	24	34
Tether length L (km)	4.02	5.77	9.27	12.9
E-sail thrust at 1 AU (N)	0.03	0.05	0.13	0.25
E-sail power $P_{\rm o} + P_{\rm eg}$ (W)	38.5	64.6	142	269
Payload idle power (W)	12.5	25.0	62.5	125
Payload duty power (W)	125	250	625	1250
Main tethers $Nm_{\rm mt}$ (kg)	0.56	1.07	2.57	5.05
Main tether reels $Nm_{\rm mr}$ (kg)	1.54	2.26	3.99	6.52
Electron guns $3m_{\rm eg}$ (kg)	0.09	0.16	0.39	0.78
HV source $m_{\rm vs}$ (kg)	0.57	1.09	2.63	5.17
Cameras and computer (kg)	1.48	1.48	1.48	1.48
Remote units $Nm_{\rm ru}$ (kg)	11.7	15.8	24.1	34.0
Auxtethers (kg)	6.83	9.80	15.8	21.9
Power system $m_{\rm sa}$ (kg)	32.0	61.6	151	299
Telemetry system (kg)	25.0	50.0	125	250
Thermal control (kg)	8.46	16.7	41.3	82.2
ACS (kg)	9.90	18.9	45.7	89.8
Structure (kg)	35.0	66.9	161	317
20 % margin (kg)	46.6	89.2	215	422
Total without E-sail (kg)	248	490	1215	2425
E-sail effective (kg)	31.7	45.1	74.1	110
Total (kg)	280	535	1290	2535
E-sail mass fraction (%)	11.4	8.44	5.74	4.34
E-sail specific acc. (mm s^{-2})	0.88	1.18	1.74	2.30

2.9 Characteristic acceleration

Using Table 1 the total spacecraft mass given by Eq. (1) can be computed in terms of four design parameters, namely N, L, V_0, $m_{\rm pay}$.

The spacecraft characteristic acceleration, that is, the maximum propulsive acceleration at a reference distance $r_\oplus$ from the Sun, can be similarly expressed as a function of the same four parameters. In fact, the thrust per unit main-tether-length at a distance of 1 AU from the Sun is (Janhunen et al., 2010)

$$f = f_V\, V_0 - f_0, \tag{12}$$

where $f_0 \equiv 24.16\,{\rm nN\,m^{-1}}$ and $f_V \equiv 24.16\,{\rm nN\,m^{-1}\,kV^{-1}}$. The spacecraft characteristic acceleration is therefore

$$a_\oplus = \frac{f\,N\,L}{m}. \tag{13}$$

3 Results

Tables 2, 3 and 4 show the spacecraft mass budget and some other fundamental parameters corresponding to a characteristic acceleration $a_\oplus$ 0.1, 0.3 and 1 mm s^{-2}. In each

Table 3. Same as Table 2, but for a characteristic acceleration $a_\oplus = 0.3\,\mathrm{mm\,s^{-2}}$.

Payload m_{pay} (kg)	100	200	500	1000
Number of tethers N	16	24	36	50
Tether length L (km)	6.38	8.02	12.7	17.9
E-sail thrust at 1 AU (N)	0.06	0.11	0.27	0.52
E-sail power $P_{\mathrm{o}} + P_{\mathrm{eg}}$ (W)	70.3	124	281	540
Payload idle power (W)	12.5	25.0	62.5	125
Payload duty power (W)	125	250	625	1250
Main tethers Nm_{mt} (kg)	1.18	2.22	5.29	10.3
Main tether reels Nm_{mr} (kg)	2.33	3.77	6.87	11.4
Electron guns $3m_{\mathrm{eg}}$ (kg)	0.18	0.34	0.81	1.59
HV source m_{vs} (kg)	1.21	2.28	5.42	10.6
Cameras and computer (kg)	1.48	1.48	1.48	1.48
Remote units Nm_{ru} (kg)	16.2	23.3	35.4	49.3
Auxtethers (kg)	10.8	13.6	21.6	30.4
Power system m_{sa} (kg)	32.0	61.6	151	299
Telemetry system (kg)	25.0	50.0	125	250
Thermal control (kg)	8.54	16.8	41.6	82.8
ACS (kg)	10.5	19.8	47.1	91.9
Structure (kg)	37.0	69.7	166	324
20% margin (kg)	49.3	93.0	221	433
Total without E-sail (kg)	248	490	1215	2425
E-sail effective (kg)	47.8	68.2	113	171
Total (kg)	296	558	1329	2596
E-sail mass fraction (%)	16.2	12.2	8.52	6.58
E-sail specific acc. ($\mathrm{mm\,s^{-2}}$)	1.24	1.64	2.35	3.04

Table 4. Same as Table 2, but for a characteristic acceleration $a_\oplus = 1\,\mathrm{mm\,s^{-2}}$.

Payload m_{pay} (kg)	100	200	300
Number of tethers N	44	62	86
Tether length L (km)	15.3	19.4	20.0
E-sail thrust at 1 AU (N)	0.39	0.70	1.00
E-sail power $P_{\mathrm{o}} + P_{\mathrm{eg}}$ (W)	409	720	1026
Payload idle power (W)	12.5	25.0	37.5
Payload duty power (W)	125	250	375
Main tethers Nm_{mt} (kg)	7.79	13.9	19.8
Main tether reels Nm_{mr} (kg)	9.21	14.8	20.8
Electron guns $3m_{\mathrm{eg}}$ (kg)	1.20	2.13	3.05
HV source m_{vs} (kg)	7.98	14.2	20.3
Cameras and computer (kg)	1.48	1.48	1.48
Remote units Nm_{ru} (kg)	43.1	59.3	77.6
Auxtethers (kg)	26.1	32.9	34.0
Power system m_{sa} (kg)	32.0	61.6	91.3
Telemetry system (kg)	25.0	50.0	75.0
Thermal control (kg)	9.31	18.1	26.9
ACS (kg)	13.8	24.7	35.3
Structure (kg)	48.9	87.0	125
20% margin (kg)	65.2	116	166
Total without E-sail (kg)	248	490	732
E-sail effective (kg)	143	206	264
Total (kg)	391	696	996
E-sail mass fraction (%)	36.6	29.6	26.5
E-sail specific acc. $\mathrm{mm\,s^{-2}}$)	2.73	3.38	3.77

case (label "Total" in the tables) the number of tethers, an even integer, was optimized for minimizing the total spacecraft mass, and the tether length was iteratively adjusted for each N until the desired characteristic acceleration was obtained. Note that the tether length was restricted to a maximum value of 20 km and the number of tethers to 100. The "Total without E-sail" values were obtained by using the same mass formula, but enforcing the conditions $N = 0$ and $L = 0$. This represents a spacecraft with the same payload mass and other functionalities, but without on-orbit propulsive capabilities. The E-sail mass fraction is the effective mass divided by the total spacecraft mass, and the E-sail specific acceleration is the propulsive thrust at 1 AU divided by its effective mass. Tables 2, 3 and 4 show some characteristic trends that can be summarized as follows.

1. When the E-sail size increases, its specific acceleration improves and the E-sail mass fraction decreases. This is because the main tether reels and RUs have, by assumption, a certain base mass even in the limit of short main and auxiliary tethers. By redesigning and miniaturizing these items, the E-sail specific acceleration could probably be improved for small sizes. On the other hand, the trend would probably not continue to even larger sizes, because for tethers longer than 20–30 km, their tensile strength requirement would start to grow beyond what Heytethers tolerate. If even longer tethers were used, thicker wires or better materials should probably be employed.

2. Tables 2 and 3 show that by moving from $0.1\,\mathrm{mm\,s^{-2}}$ to $0.3\,\mathrm{mm\,s^{-2}}$ of characteristic acceleration, the E-sail's mass fraction increases only slightly. For example, for a 1000 kg of payload, the spacecraft total mass is about 2535 kg when $a_\oplus = 0.1\,\mathrm{mm\,s^{-2}}$, while it is 2596 kg (only 2.4 % larger) for a three times more capable system ($a_\oplus = 0.3\,\mathrm{mm\,s^{-2}}$). In light of these numbers and assuming the availability of E-sails of different sizes, using the lowest characteristic acceleration ($a_\oplus = 0.1\,\mathrm{mm\,s^{-2}}$) might be motivated only if the spacecraft payload is of some bulk material, such as products from asteroid mining, rather than a technical payload.

3. Currently, RUs, auxiliary tethers, main tethers, main tether reels, and the HV subsystem all significantly contribute to the E-sail's effective mass.

For comparative purposes, Table 5 shows the mass breakdown for a spacecraft having the same parameters of Table 4 with the exception that in Table 5 the auxiliary tethers are made of 7.6 µm Kapton (instead of 12.7 µm) and that the cold

Table 5. Same as Table 4, but with thinner auxiliary tethers (7.6 µm) and RUs with cold gas thrusters.

Payload $m_{\rm pay}$ (kg)	100	200	300
Number of tethers N	38	56	80
Tether length L (km)	15.6	19.5	19.9
E-sail thrust at 1 AU (N)	0.34	0.63	0.92
E-sail power $P_{\rm o} + P_{\rm eg}$ (W)	360	657	950
Payload idle power (W)	12.5	25.0	37.5
Payload duty power (W)	125	250	375
Main tethers $Nm_{\rm mt}$ (kg)	6.83	12.6	18.4
Main tether reels $Nm_{\rm mr}$ (kg)	8.02	13.4	19.3
Electron guns $3m_{\rm eg}$ (kg)	1.05	1.94	2.82
HV source $m_{\rm vs}$ (kg)	7.00	12.9	18.8
Cameras and computer (kg)	1.48	1.48	1.48
Remote units $Nm_{\rm ru}$ (kg)	24.5	34.7	46.3
Auxtethers (kg)	15.8	19.9	20.2
Power system $m_{\rm sa}$ (kg)	32.0	61.6	91.3
Telemetry system (kg)	25.0	50.0	75.0
Thermal control (kg)	9.19	18.0	26.8
ACS (kg)	12.2	22.4	32.6
Structure (kg)	42.9	79.2	115
20% margin (kg)	57.2	106	154
Total without E-sail (kg)	248	490	732
E-sail effective (kg)	95.2	144	190
Total (kg)	343	634	922
E-sail mass fraction (%)	27.7	22.7	20.6
E-sail specific acc. (mm s^{-2})	3.60	4.40	4.85

gas thruster option is taken into account. Recall that the wet mass of the cold gas unit is 0.267 kg lighter than the FEEP version. The mass of a RU with cold gas thrusters can also be representative of a solar photon blade equipped version of the RU, which has sufficient spin rate control capability for any mission (Janhunen, 2012). Making the auxiliary tethers thinner, favours longer tethers in the mass optimization process, while a reduced RU base mass has the opposite effect. Because the numbers of tethers in Table 5 are smaller than those in Table 4, a reduction of the auxiliary tether thickness has a larger impact than that of changing the RU's thruster class. For the 300 kg payload case, the net result is a 28% reduction in the E-sail effective mass and a corresponding increase in the E-sail specific acceleration.

We have thus far assumed that the nominal tether voltage V_0 (valid for average solar wind conditions) has a fixed value of 25 kV. The maximum voltage for which the hardware is designed should be larger, perhaps 40 kV, because otherwise the thrust would be decreased when the solar wind density is lower than its average value (Toivanen and Janhunen, 2009). Trading off the hardware voltage limit against other design parameters is outside the scope of this paper, although we will explore the effect of the value of V_0 at the end of this section.

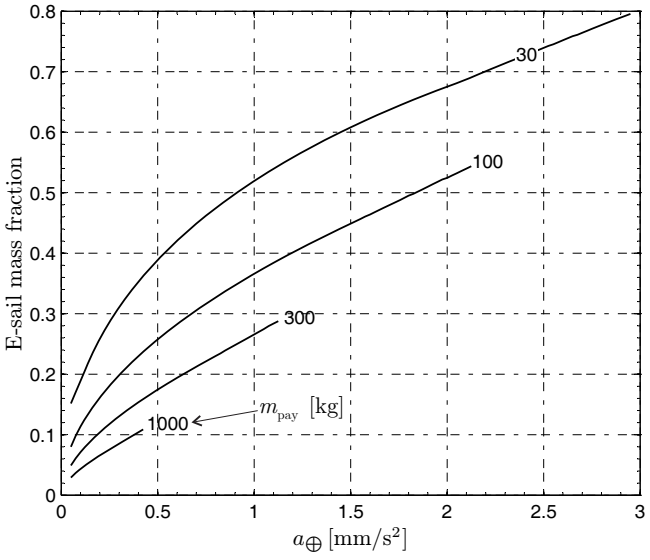

Fig. 4. E-sail mass fraction as a function of $a_\oplus$ and $m_{\rm pay}$.

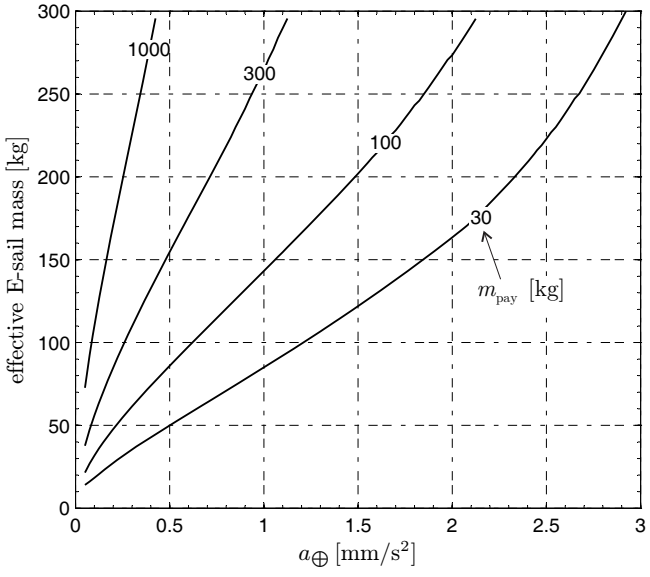

Fig. 5. Effective E-sail mass as a function of $a_\oplus$ and $m_{\rm pay}$.

Figure 4 shows the E-sail mass fraction (effective E-sail mass divided by spacecraft total mass) as a function of the characteristic acceleration, for different payloads $m_{\rm pay}$ of 30, 100, 300 and 1000 kg. For each payload mass, there exists a maximum characteristic acceleration that can be reached by an E-sail. Recall that, by assumption, the E-sail performance is constrained by a maximum number (100) and length (20 km) of main tethers.

Figures 5–7 illustrate the corresponding effective E-sail mass, total spacecraft mass and E-sail propulsive thrust, respectively. Figures 4–7 span a wide range of potential applications. Small values of characteristic accelerations with a

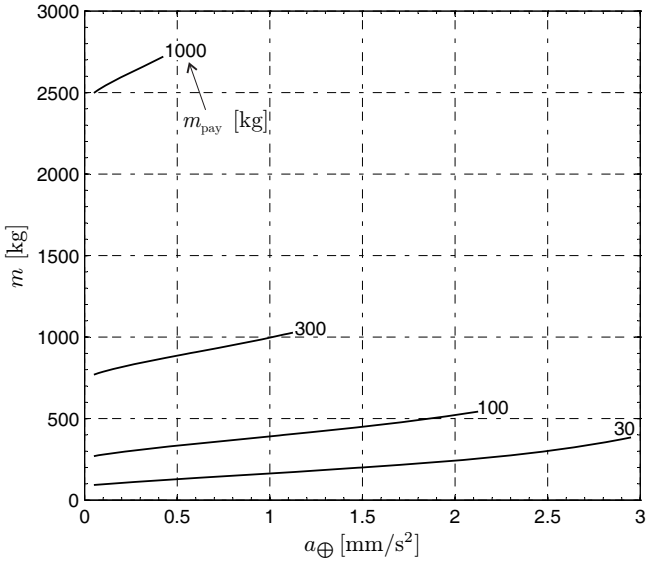

Fig. 6. Spacecraft total mass as a function of $a_\oplus$ and $m_{\rm pay}$.

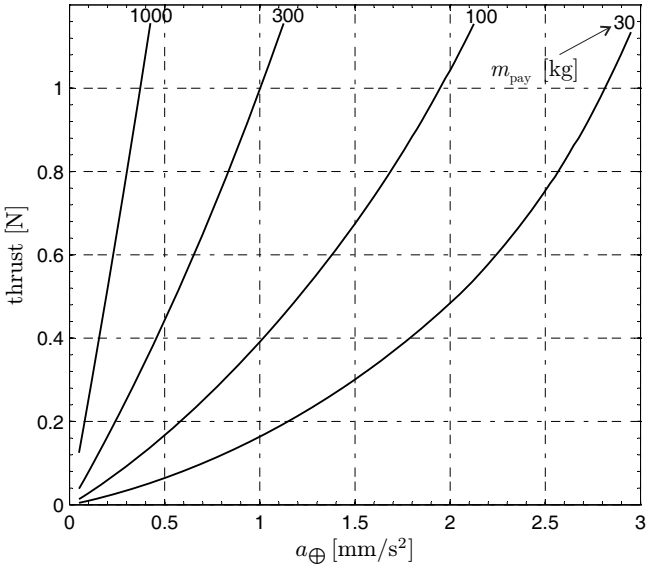

Fig. 7. E-sail thrust at 1 AU as a function of $a_\oplus$ and $m_{\rm pay}$.

30 kg payload correspond to a small, first-generation E-sail, perhaps suitable for the near-term applications. The upper limits of the level curve with $m_{\rm pay} = 30$ kg correspond, instead, to a high-performance E-sail for an advanced mission scenario as, for instance, a flyby with outer planets or a Solar System escape. On the other side, the low $a_\oplus$ end of the level curve with $m_{\rm pay} = 1000$ kg represents a case where a 2.5 t spacecraft is moved at 0.1 mm s^{-2} characteristic acceleration (3 km s^{-1} of Δv per year) by a moderate size 34-tether E-sail weighing 110 kg (Table 2). The latter case is consistent, for example, with an advanced exploration mission towards near-Earth asteroids, which involves an in situ resource utilization and transportation (see Lewis, 1996; Gerlach, 2005).

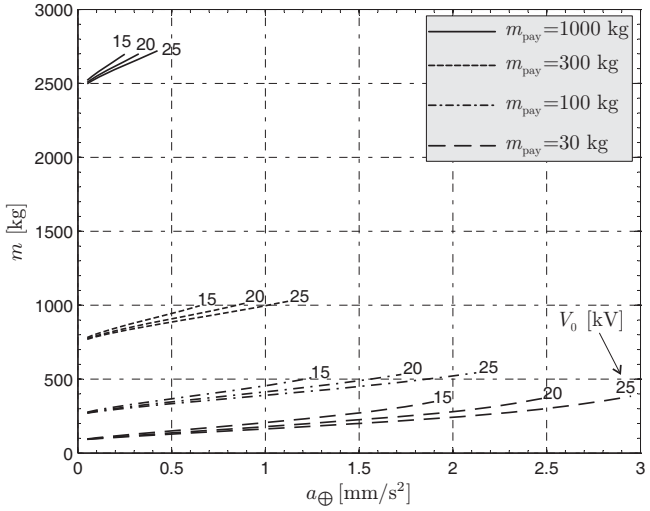

Fig. 8. Spacecraft total mass as a function of $a_\oplus$ and $m_{\rm pay}$, for three values of V_0: 15, 20 and 25 kV.

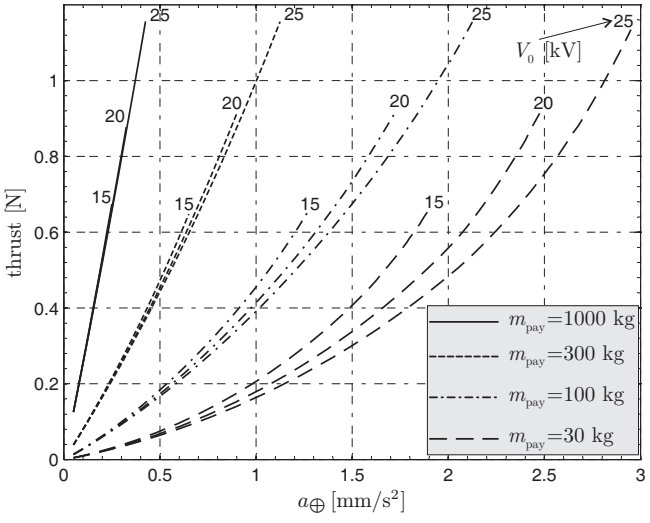

Fig. 9. E-sail thrust at 1 AU as a function of $a_\oplus$ and $m_{\rm pay}$, for three values of V_0: 15, 20 and 25 kV.

3.1 Dependence on employed voltage

The high voltage V_0 employed at normal solar wind conditions was thus far fixed at 25 kV. We now briefly explore what happens if this value is altered. Figure 8 is similar to Fig. 6, but it shows the total mass of the spacecraft not only as a function of the characteristic acceleration $a_\oplus$ and payload mass $m_{\rm pay}$, but also for three different values of V_0, namely 15, 20 and 25 kV. It is seen that lowering the voltage from 25 kV has only a minor effect on the spacecraft total mass in each case. The main effect shown in Fig. 8 is that the curves with lower V_0 end earlier. The reason is that the highest achievable characteristic acceleration depends on V_0 because the thrust per unit tether length depends on it and, by

assumption, the maximum tether length is limited to 20 km while the maximum number of tethers is 100.

Figure 9 is a generalization of Fig. 7 showing the thrust as a function of $a_{\oplus}$, m_{pay} and V_0. Again, the effect of varying V_0 is not too significant except that the curves for lower V_0 end earlier because of the assumed total tether length limitation.

4 Conclusions

A detailed mathematical model has been developed for mass budget analysis and performance evaluation of an E-sail spacecraft. Our aim was to estimate the component masses as realistically as possible with current or near-term technology while including a conservative 20 % overall mass margin.

Accurate mass estimates of a propulsion system are difficult to obtain, because the thruster design has usually indirect effects on other spacecraft subsystems as, for instance, the thermal and the attitude control systems. In this paper we have estimated the effective E-sail mass by evaluating the mass difference between the actual and a virtual spacecraft. The latter has the same functional components and satisfies the same environmental requirements of the former, but lacks propulsive capabilities. In that way, the indirect mass contributions are included in the estimation.

Numerical results show that the E-sail propulsion system, once qualified for flight, could be an interesting option for a wide class of deep space missions that include payloads in the range 30–1000 kg, and require a characteristic acceleration up to about $3\,\mathrm{m\,s^{-2}}$. Moreover, as is shown in Table 5, some rather straightforward near-term component level improvements have the potential of reducing the effective E-sail mass further (28 % in the specific case) with a consequent improvement in mission performance. Future work will concentrate on prototyping and testing the E-sail subsystem as well as measuring the E-sail performance on a small scale in the real environment, that is, within the solar wind.

Acknowledgements. This research was financed within the European Community's Seventh Framework Programme ([FP7/2007-2013]) under grant agreement number 262733 and the Academy of Finland grant decision 250591.

Edited by: H. Svedhem

References

Gerlach, C. L.: Profitably exploiting near-Earth object resources, International Space Development Conference, Washington DC, 2005, available at: http://abundantplanet.org/files/Space-Ast-Profitably-Exploiting-NEO-Gerlach-2005.pdf (last access: 14 March 2012), 2005.

Hoyt, R. and Forward, R.: Alternate interconnection hoytether failure resistant multiline tether, US Pat. 6286788, filed: 8 September, 2000.

Janhunen, P.: Electric sail for producing spacecraft propulsion, US Pat. 7641151, accepted 2010, filed: 2 March, 2006.

Janhunen, P.: Increased electric sail thrust through removal of trapped shielding electrons by orbit chaotisation due to spacecraft body, Ann. Geophys., 27, 3089–3100, doi:10.5194/angeo-27-3089-2009, 2009.

Janhunen, P.: Photonic spin control for solar wind electric sail, Acta Astronautica, 83, 85–90, 2013.

Janhunen, P., Toivanen, P. K., Polkko, J., Merikallio, S., Salminen, P., Haeggstrom, E., Seppänen, H., Kurppa, R., Ukkonen, J., Kiprich, S., Thornell, G., Kratz, H., Richter, L., Krömer, O., Rosta, R., Noorma, M., Envall, J., Lätt, S., Mengali, G., Quarta, A. A., Koivisto, H., Tarvainen, O., Kalvas, T., Kauppinen, J., Nuottajärvi, A., and Obraztsov, A.: Electric solar wind sail: Towards test missions, Rev. Sci. Instrum., 81, 111301-1–111301-11, doi:10.1063/1.3514548, 2010.

Kurppa, R., Ukkonen, J., Kiprich, S., Seppänen, H., Janhunen, P., and Haeggström, E.: Method for electric solar wind sail tether production, European Planetary Science Congress, Paper EPSC 2010-294, Rome, Italy, 19–24 September, 2010.

Larson, W. J. and Wertz, J. R.: Space mission analysis and design, 3rd Edn., Kluwer, ISBN:1-881-88310-8, 1999.

Lewis, J. S.: Mining the sky: Untold riches from the asteroid, comets, and planets, Addison-Wesley, ISBN:0-201-32819-4, 1996.

Marcuccio, S., Giusti, N., and Pergola, P.: Development of a miniaturized electric propulsion system for the E-sail project, 62nd International Astronautical Congress, Paper IAC-11.B4.6A.3, 2011.

McInnes, C. R.: Solar sailing: Technology, dynamics and mission applications, 46–54, Springer-Verlag, ISBN:3-540-21062-8, 1999.

Mengali, G., Quarta, A. A., and Janhunen, P.: Electric sail performance analysis, J. Spacecraft Rockets, 45, 122–129, doi:10.2514/1.31769, 2008.

Näsilä, A., Hakkarainen, A., Kestilä, A., Nordling, K., Modrzewski, R., Praks, J., Hallikainen, M., Saari, H., Antila, J., Mannila, R., Janhunen, P., and Vainio, R.: Aalto-1 – a hyperspectral Earth observing nanosatellite, SPIE Remote Sensing, Prague, Czech Republic, 19–22 September 2011, doi:10.1117/12.898125, 2011.

Nemzek, R. J. and Winckler, J. R.: Electron beam sounding rocket experiments for probing the distant magnetosphere, Phys. Rev. Lett., 67, 987–990, doi:10.1103/PhysRevLett.67.987, 1991.

Pajusalu, M., Rantsus, R., Pelakauskas, M., Leitu, A., Ilbis, E., Kalde, J., Lillmaa, H., Reinumägi, R., Voormansik, K., Zālite, K., Allik, V., Noorma, M., and Lätt, S.: Design of the electric power system for the ESTCube-1 satellite, Latv. J. Phys. Tech. Sci., 3, 16–24, doi:10.2478/v10047-012-0014-4, 2012.

Pappa, R. S., Blandino, J. R., Caldwell, D. W., Carroll, J. A., Jenkins, C. H. M., and Pollock, T. C.: Optical diagnostic system for solar sails: Phase 1 final report, NASA/TM-2004-213511, 2004.

Praks, J., Kestilä, A., Hallikainen, M., Saari, H., Antila, J., Janhunen, P., and Vainio, R.: Aalto-1 – an experimental nanosatellite for hyperspectral remote sensing, Geoscience and Remote Sensing Symposium (IGARSS), IEEE International, Vancouver, Canada, 25–29 July 2011, doi:10.1109/IGARSS.2011.6050199,

2011.

Quarta, A. A. and Mengali, G.: Electric sail mission analysis for outer Solar System exploration, J. Guid. Control Dynam., 33, 740–755, doi:10.2514/1.47006, 2010.

Quarta, A. A., Mengali, G., and Janhunen, P.: Optimal interplanetary rendezvous combining electric sail and high thrust propulsion system, Acta Astronaut., 68, 603–621, doi:10.1016/j.actaastro.2010.01.024, 2011.

Seppänen, H., Kiprich, S., Kurppa, R., Janhunen, P., and Haeggström, E.: Wire-to-wire bonding of µm-diameter aluminum wires for the Electric Solar Wind Sail, Microelectron. Eng., 88, 3267–3269, doi:10.1016/j.mee.2011.07.002, 2011.

Toivanen, P. K. and Janhunen, P.: Electric sailing under observed solar wind conditions, Astrophys. Space Sci. Trans., 5, 61–69, doi:10.5194/astra-5-61-2009, 2009.

Toivanen, P. K. and Janhunen, P.: Spin plane control and thrust vectoring of electric solar wind sail by tether potential modulation, J. Propul. Power, 29, 178–185, doi:10.2514/1.B34330, 2013.

Wagner, S., Sundqvist, J., and Thornell, G.: Design description of the Remote Unit, ESAIL EU FP7 project deliverable D41.2, available at: http://www.electric-sailing.fi/fp7/docs/D412.pdf, 2012.

Wright, J. L.: Space sailing, 223–226, Gordon and Breach Science Publisher, ISBN:2-881-24842-X, 1992.

Zavyalov, M. A., Tujrujkanov, P. M., and Evlanov, E. N.: Solar ion sail electron gun study, Parts 1-2, Internal contract report of IKI/Moscow to FMI/Helsinki, 2006.

APPENDIX 2 [AD6]

Toivanen, P. and P. Janhunen, “*Spin plane control and thrust vectoring of electric solar wind sail by tether potential modulation*”, J. Prop. Power, 29, 178-185, 2013

Spin Plane Control and Thrust Vectoring of Electric Solar Wind Sail by Tether Potential Modulation

Petri K. Toivanen[1] and Pekka Janhunen
Finnish Meteorological Institute, Helsinki, FIN-00560, Finland

The electric solar wind sail is a propulsion system that uses long centrifugally spanned and electrically charged tethers to extract the solar wind momentum for spacecraft thrust. The sail angle with respect to the sun direction can be controlled by modulating the voltage of each tether separately to produce net torque for attitude control and thrust vectoring. A solution for the voltage modulation that maintains any realistic sail angle under constant solar wind is obtained. Together with the adiabatic invariance of the angular momentum, the tether spin rate and coning angle is solved as functions of temporal changes in the solar wind dynamic pressure, the tether length, or the sail angle. The obtained modulation also gives an estimate for the fraction of sail performance (electron gun power) to be reserved for sail control. We also show that orbiting around the Sun with a fixed sail angle leads to a gradual increase (decrease) in the sail spin rate when spiraling outward (inward). This effect arises from the fact that the modulation of the electric sail force can only partially cancel the Coriolis effect, and the remaining component lays in the spin plane having a cumulative effect on the spin rate.

---

[1] Finnish Meteorological Institute, Earth Observation, P.O. Box 503, FIN-00101, Helsinki, Finland

Nomenclature

A = tether wire cross-sectional area

α = sail angle

$\mathbf{e}$ = unit vector

$\mathbf{F}$ = force

g = tether voltage modulation

I = tether moment of inertia

l = tether length

$\mathbf{L}$ = angular momentum

Λ = sail coning angle

m_p = proton mass

n_{w} = solar wind number density

$\boldsymbol{\omega}$ = angular velocity

$\widetilde{\omega}$ = angular frequency

$\boldsymbol{\Omega}$ = angular velocity of sail turning

P_{dyn} = solar wind dynamic pressure

(r, θ, φ) = spherical polar coordinates

ρ_l = tether material linear mass density

ρ_V = tether material mass density

T = tether root tension

$\boldsymbol{\tau}$ = torque

$(\theta_{\mathrm{w}}, \varphi_{\mathrm{w}})$ = solar zenith angles

$\mathbf{u}$ = solar wind velocity

V = tether voltage

$\mathbf{v}$ = velocity

I. Introduction

The electric solar wind sail was proposed in [1] as a propulsion system that uses the ambient interplanetary solar wind momentum flux for spacecraft thrust as inspired by the earlier magnetic sail concept in [2]. The proposed electric sail consisted of a conducting mesh charged to a high positive potential to repel the solar wind ions. Later, it was recognized that centrifugally stretched micro-meteoroid resistant tethers [3] can be used to construct the sail [4, 5]. It was noticed that an electric field potential structure of the spatial range larger than 100 m can be created around a thin wire with thickness of a few tens of micrometers. While such a construction provided a lightweight sail with an effective area comparable to a mesh, it also suggested a convenient way both to open the sail in space by reeling out the tethers instead of unfolding the mesh and also to control the sail spin plane by modulating the voltage of the electrically independent tethers.

The flight attitude control of a single tether and collectively the sail is a key challenge in electric sail development. Recently, it was shown that if attitude control is accomplished, the navigation in real solar wind conditions to planetary targets with an electric sail is feasible [6]. The sail inclination with respect to the sun-direction can be controlled and altered by modulating the individual tether voltage synchronously with the sail rotation, resembling helicopter flight from the algorithmic point of view. Since the tethers are much longer (up to tens of kilometers) than any realistic spacecraft radius, the rotation phase of the tether is not stabilized by the centrifugal force as is the case for the helicopter blades attached to the central plate. Initially, it was envisioned that the individual tether rotation rate can be controlled by varying the tether length by reeling. This would necessitate mechanical moving bodies, and as a more attractive option, auxiliary tethers connecting the tether tips can be added for mechanical stability to the baseline configuration [7].

The existing thrust law for an infinitely long positively charged electric sail tether is based on the studies in [5] and [8]. In general, the thrust force is proportional to the solar wind dynamic pressure and the effective area of the sail and its direction is along the component of the solar wind that is perpendicular to the tether. The latter feature is a key difference in comparison with the solar sail for which the thrust is perpendicular to the sail surface (assuming fully reflecting sail material). Since the tether voltage is much higher than the electron temperature, the Debye

length is not necessarily the scale size of the tether potential structure. Initially, a particle-in-cell computer simulation was used to predict the thrust law [5]. Based on these simulation results, the potential structure scale size is of the order of hundred meters. Later, it was noted that due to the complex electric field structures near the spacecraft, the electron motion becomes chaotic and the electrons trapped by the wire will be scattered [8]. Such a mechanism effectively removes the trapped electrons. This is, however, difficult to take into account self-consistently in the original simulation, and an analytical solution for the thrust law was constructed in [8]. It was argued that the analytic solution is in good agreement both with the simulation results (except that the thrust is about 5 times larger than that based on the simulations) and with the study by [9]. Concerning the present work, since the rotation rate of the sail is a free parameter, possible ambiguities of the thrust law do not invalidate the results of this paper that depend only on the ratio of the electric sail and centrifugal forces, i.e., the coning angle of the sail.

The electric sail tether dynamics and control includes a rotating body in a frame of reference rotating along with the sail orbiting around the Sun and introducing effects to the tether rotation period not necessarily intuitive in the framework of a freely swinging spherical pendulum. In Section 2, we introduce the electric sail thrust law together with coordinate systems to derive the single tether equation of motion. At this stage, it is adequate to consider a single tether as the Coulomb interaction between the tethers is weak due to the plasma shielding of the tether potential structures. An analytic solution for the tether voltage modulation for any tether spin plane orientation relevant for sail operations is obtained in Section 3 where we also give examples of variation in electric sail force and tether length tuning. The Coriolis effect is considered in Section 4 and examples of turning of the sail spin plane together with the result of the sail spin period evolution with controlled orbiting around the Sun are shown. In Sections 3 and 4, we give both the exact analytic solutions and their approximations for small coning angles. The results and implications to electric sail control and performance are summarized in Section 5. Limitations of the tether model used in this paper are also discussed in terms of realistic flexible tethers and variable solar wind conditions.

II. Electric sail tether motion

A. Thrust law

The magnitude of the force per tether length is given in [7] as

$$\frac{dF_u}{dz} \approx 0.18 \max(0, V - V_{\rm w})\sqrt{\epsilon_0 P_{\rm dyn}}, \tag{1}$$

where V is the tether voltage, $V_{\rm w}$ is the electric potential ($m_p u^2/2e$) corresponding to the kinetic energy of the solar wind ions, and $P_{\rm dyn}$ is the dynamic pressure of the solar wind, $P_{\rm dyn} = m_p n_{\rm w} u^2$. In Equation (1), $n_{\rm w}$ and u are the solar wind number density and flow speed, respectively. As the force exerted to the tether by the solar wind is perpendicular to the tether, the tether thrust vector is written as

$$\frac{d\mathbf{F}_u}{dz} = \xi \mathbf{u}_\perp, \tag{2}$$

where $\xi = 0.18 \max(0, V - V_{\rm w})\sqrt{\epsilon_0 m_p n_{\rm w}}$. Concerning the results of this paper, the exact value of ξ is not critical. The sail spin period is a free parameter that can be adapted so that the solar wind force is a desirable fraction of the tether centrifugal force corresponding to the tangent of the tether coning angle (Figure 1b) that defines the sail dynamics. The electric sail thrust integrated over the sail tethers points approximately to the median direction ($\mathbf{f}_u$) of the solar wind ($\mathbf{u}$) and sail normal ($\mathbf{n}$) directions as shown in Figure1a. This is a difference between the electric sail and the photon sail for which the thrust is normal to the sail surface.

B. Coordinate systems

For further analysis, we define two coordinate systems. Both systems are sail-centric with the Y axis being perpendicular to the solar ecliptic plane. The one shown in Fig 1a, the Sail-centric Solar Ecliptic (SSE) system has the Z axis pointing to the Sun, and the X axis completing the right handed triad. The other, the Sail Ecliptic (SE) system (Fig 1b) is obtained by rotating the SSE coordinates by the sail angle (α) with respect to the Y axis. As implied by the name, the SSE system is analogous to the Geocentric Solar Ecliptic (GSE) system, except that $X_{\rm SSE}$ = -$Y_{\rm GSE}$, $Y_{\rm SSE}$ = -$Z_{\rm GSE}$, and $Z_{\rm SSE}$ = $X_{\rm GSE}$. Note that the definition of these coordinate systems in traditional terms of the ecliptic plane is arbitrary, and the ecliptic plane can also be considered as the sailcraft orbital plane.

The analysis of the temporal evolution of the tether key variables, coning angle and rotation rate, is simplest in the spherical SE coordinates as the desired sail orientation corresponds to the solution of constant polar angle ($\dot{\theta}_{\mathrm{SE}} = 0$). Since the SE system is not inertial, fictitious forces arising from the Coriolis

$$\mathbf{F}_C = -2m\,\boldsymbol{\Omega} \times \mathbf{v}, \tag{3}$$

centripetal ($\mathbf{F}_{cp} = -m\,\boldsymbol{\Omega} \times (\boldsymbol{\Omega} \times \mathbf{r})$), and Euler ($\mathbf{F}_E = -m\,\dot{\boldsymbol{\Omega}} \times \mathbf{r}$) effects have to be taken into account. In general, $\mathbf{r}$ and $\mathbf{v}$ are the particle position and velocity vectors in a reference frame rotating with an angular velocity vector $\boldsymbol{\Omega}$. In this study, $\boldsymbol{\Omega}$ is determined either by the turning of the sail spin plane or by the orbital motion around the Sun. Since the angular frequency of the sail rotation is much higher than that of the SE system, the centripetal and Euler effects can be neglected as being of the second order in Ω.

C. Equation of motion

The equation of the tether motion can be obtained from

$$\frac{d\mathbf{L}}{dt} = \frac{d}{dt}\left(I\boldsymbol{\omega}\right) = \boldsymbol{\tau}_{\mathrm{w}} + \boldsymbol{\tau}_C \tag{4}$$

as expressed in terms of the tether angular momentum ($\mathbf{L}$), angular velocity ($\boldsymbol{\omega}$), the moment of inertia (I), and torques arising from the electric sail force ($\boldsymbol{\tau}_{\mathrm{w}}$) and Coriolis effect ($\boldsymbol{\tau}_{\mathrm{C}}$). For a thin tether wire,

$$I = \frac{1}{3}\rho_V A l^3, \tag{5}$$

where ρ_V is the mass density of the tether material, A is the cross-sectional area of the wire, and l is the tether length. Using Equation (2), $\boldsymbol{\tau}_{\mathrm{w}}$ is integrated over the tether length as

$$\begin{aligned} \boldsymbol{\tau}_{\mathrm{w}} &= \int_0^l \mathbf{r} \times d\mathbf{F}_{\mathrm{u}} \\ &= \frac{1}{2}\xi l^2(-u_\varphi \mathbf{e}_\theta + u_\theta \mathbf{e}_\varphi), \end{aligned} \tag{6}$$

where

$$\begin{aligned} u_\theta &= u_x \cos\theta\cos\varphi + u_y \cos\theta \sin\varphi - u_z \sin\theta \\ u_\varphi &= -u_x \cos\varphi + u_y \cos\varphi \end{aligned} \tag{7}$$

are the spherical components of the solar wind, and l is the tether length. Defining the tether velocity in spherical coordinates, the torque caused by the Coriolis effect (3) can be integrated over the tether length as in (6) as

$$\begin{aligned}\boldsymbol{\tau}_C &= \int_0^l 2\rho_l(\mathbf{r}\cdot\boldsymbol{\Omega})\mathbf{v}dr \\ &= 2I\Omega\sin\theta\sin\varphi(\dot{\theta}\mathbf{e}_\theta + \sin\theta\dot{\varphi}\mathbf{e}_\varphi),\end{aligned} \tag{8}$$

where any terms including possible tether length time variation have been neglected, and ρ_l is the tether mass per unit length. Here, we assumed that the sail is orbiting on the ecliptic plane and tilted as shown in Figure 1a, and $\boldsymbol{\Omega} = \Omega\mathbf{e}_y$. The angular velocity in Equation (4) can be solved from $\mathbf{v} = \boldsymbol{\omega}\times\mathbf{r}$ to read as

$$\boldsymbol{\omega} = -\sin\theta\dot{\varphi}\mathbf{e}_\theta + \dot{\theta}\mathbf{e}_\varphi. \tag{9}$$

For further manipulation of the equation of motion (4), we express the solar wind velocity in terms of the zenith angles of its nominal direction (θ_w and φ_w) as

$$\begin{aligned}u_\theta &= u\left(\sin\theta_\mathrm{w}\cos\theta\cos(\varphi-\varphi_\mathrm{w}) - \cos\theta_\mathrm{w}\sin\theta\right) \\ u_\varphi &= -u\sin\theta_\mathrm{w}\sin(\varphi-\varphi_\mathrm{w})\end{aligned} \tag{10}$$

defined by

$$\begin{aligned}u_x &= u\sin\theta_\mathrm{w}\cos\varphi_\mathrm{w} \\ u_y &= u\sin\theta_\mathrm{w}\sin\varphi_\mathrm{w} \\ u_z &= u\cos\theta_\mathrm{w}.\end{aligned} \tag{11}$$

For completeness of the equation of motion, the solar wind zenith phase angle is explicitly left here although $\varphi_\mathrm{w} = 0$ for the case considered in this study. After these definitions, taking the time derivative and rearranging the spherical vector components, we write the equation of motion as

$$\begin{aligned}l^3\sin\theta\cos\theta\,\dot{\varphi}^2 &= -g\lambda l^2\left(\sin\theta_\mathrm{w}\cos\theta\cos(\varphi-\varphi_\mathrm{w}) - \cos\theta_\mathrm{w}\sin\theta\right) \\ &\quad -2\Omega l^3\sin^2\theta\sin\varphi\dot{\varphi} \\ &\quad +\frac{d}{dt}\left(l^3\dot{\theta}\right)\end{aligned} \tag{12}$$

$$\frac{d}{dt}\left(l^3\sin^2\theta\dot{\varphi}\right) = -g\lambda l^2\sin\theta_{\rm w}\sin\theta\sin\varphi$$
$$+2\Omega l^3\sin^2\theta\sin\varphi\dot{\theta}, \tag{13}$$

where

$$\lambda = \frac{3\xi u}{2\rho_l}. \tag{14}$$

In Equations (12) and (13) we have explicitly added the tether voltage modulation g. In addition to the tether key variables, it is important to consider the tension at the root of the tether as

$$T = \rho_V\left(\frac{1}{2}l^2\left(\dot{\theta}^2+\sin^2\theta\dot{\varphi}^2\right)-\frac{d}{dt}\left(l\dot{l}\right)\right) \tag{15}$$

for the diagnostics. While the equation of motion (12 and 13) is written for an arbitrary solar wind direction including also possible non-radial components, the rest of the paper deals with a constant solar wind and sail orbit on the ecliptic plane, and $\theta_{\rm w}=\alpha$ and $\varphi_{\rm w}=0$.

III. Solution for fixed tether spin plane ($\Omega = 0$)

In general, the tether attitude control can be addressed by the tether voltage modulation g introduced in the equation of motion (12) and (13). The tether spin plane can then be fixed to correspond to any relevant sail pointing angle with a voltage modulation that attempts to maintain $\dot{\theta}$ at zero in SE coordinates (Figure 1b). This can be done either numerically ($g=g_n$) or analytically ($g=g_a$). In the former case, the modulation can be realized by a linear controller

$$g_n = 1+c_n\dot{\theta} \tag{16}$$

that monitors the latitudinal speed $\dot{\theta}$ and corrects the tether voltage if $\dot{\theta}$ deviates from zero. For constant solar wind, an analytic form for the modulation exists depending only on the tether rotation phase: Inserting a modulation of

$$g_a(\varphi) = c_a\left(\sin\alpha\cos\theta\cos\varphi-\cos\alpha\sin\theta\right)^{-3} \tag{17}$$

in the equation of motion (12) and(13), it can be seen that $\dot{\theta}=0$. The constant c_a can be fixed by normalizing the angular average of $g_a(\varphi)$ to unity,

$$< g_a(\varphi) >_\varphi = \frac{1}{2\pi}\int_0^{2\pi} g(\varphi)d\varphi = 1. \tag{18}$$

The integral has a closed form and can be determined by partial integration. After this normalization, the modulation can be written as

$$g_a(\varphi) = \frac{2\left(1-\chi^2\right)^{5/2}}{\left(2+\chi^2\right)\left(1+\chi\cos\varphi\right)^3} \tag{19}$$

$$\approx 1 - 3\chi\cos\varphi + \mathcal{O}(\tan^2\Lambda), \tag{20}$$

where $\chi = \tan\alpha\tan\Lambda$, and the approximation (20) is for small coning angles. When considering the voltage source design of the electric sail, (19) implies that the voltage has to include design margin by a factor of

$$\max(g_a(\varphi)) = \frac{2\left(1-\chi^2\right)^{5/2}}{\left(2+\chi^2\right)\left(1-|\chi|\right)^3} \tag{21}$$

reserved for the modulator (Figure 2). It can be concluded that the larger the sail angle and the coning angle (slower spin rate) are the larger amplitude modulation is needed for the tether control.

Applying the analytic modulation (19) in Equations (12) and (13), it can be shown that the coning angle (Λ) depends on the average angular frequency ($\widetilde{\omega} =< \dot{\varphi} >_\varphi$) as

$$\widetilde{\omega}^2 = \frac{2\lambda\cos\alpha\left(1-\chi^2\right)^{3/2}}{l\sin\Lambda\left(2+\chi^2\right)} \tag{22}$$

$$\approx \frac{\lambda\cos\alpha}{l\sin\Lambda}\left(1+\mathcal{O}(\tan^2\Lambda)\right). \tag{23}$$

Taking angular average of (13), it can be seen that

$$\frac{d}{dt}\left(l^3\widetilde{\omega}\cos^2\Lambda\right) = 0 \tag{24}$$

$$\frac{d}{dt}\left(l^3\widetilde{\omega}\right) \approx \mathcal{O}(\tan^2\Lambda) \tag{25}$$

implying that $l^3\widetilde{\omega}\cos^2\Lambda$ is an adiabatic invariant of motion. Using Equations (22) and (24), $\widetilde{\omega}$ and Λ can be solved as functions of time corresponding to a given temporal change of λ and l as shown in examples below.

A. Example: Variations in electric sail force

Variations in the electric sail force are caused by the tether voltage or solar wind conditions. Using Equations (22) and (24), the coning angle and angular frequency can be solved as functions of the relative electric sail force (λ/λ_0) as shown in Figures 3a and 3b, respectively. The curves shown

are for five initial coning angles ranging from 2° to 10° spaced by 2 degrees. Based on (24) for a constant tether length, the force variations have relatively weak effect on the angular frequency.

B. Example: Tether length tuning

The tether length tuning can be used to vary the tether rotation rate as predicted by (22) and (24). Figure 4 shows the coning angle and angular frequency as functions of the tether length (l) relative to the initial length (l_0). These are shown for five initial coning angles ranging from 2° to 10° spaced by 2 degrees. As implied by Figure (4b), the approximate (25) holds well and

$$\widetilde{\omega} = \widetilde{\omega}_0 \left(\frac{l_0}{l} \right)^3 . \tag{26}$$

IV. Solution for rotating tether spin plane ($\Omega \neq 0$)

Solving the equation of motion (12) and (13) for a non-zero $\Omega << \widetilde{\omega}$, assumes an additional variation (δg) in the voltage modulation, $g \rightarrow g + \delta g$ with $\delta g << g$. Inserting such a modulation in (12) and using (22), δg as a function of the phase angle can be written as

$$\delta g = -\frac{2\Omega l \widetilde{\omega} \sin\theta \sin\varphi}{\lambda \cos\alpha \left(1 + \chi \cos\varphi\right)}. \tag{27}$$

Inserting δg in (13) and considering only angular averaged quantities, the time variation of the angular momentum is written as

$$\begin{aligned} \frac{d}{dt}\left(l^3 \widetilde{\omega} \cos^2\Lambda\right) &= 2l^3 \Omega \widetilde{\omega} \tan\alpha \cos^2\Lambda \left\langle \frac{\sin^2\varphi}{(1+\chi\cos\varphi)} \right\rangle_\varphi \\ &\approx l^3 \Omega \widetilde{\omega} \tan\alpha \cos^2\Lambda + \mathcal{O}(\tan^2\Lambda) \end{aligned} \tag{28}$$

after expanding $(1 + \chi\cos\varphi)^{-1}$ in χ, noting that $< \sin^2\varphi >_\varphi = 1/2$, and $< \sin^2\varphi \cos\varphi >_\varphi = 0$.

A. Example: Turning of the sail spin plane

Figure 5 shows a controlled turn of the sail spin plane with the initial sail angle changing from $\alpha = 0°$ to $\alpha = 45°$ as a function of time $\alpha(t)$ as shown in Figure 6a. This steering signal is then used to alter the reference signal (19) of the voltage modulation. Finally, the tether variables are transformed to the system rotated by $\alpha(t)$ and the control (16) applied in the rotated frame. Note that the sail can be turned to any orientation ($\varphi_w \neq 0$) by using the tether phase as another steering

signal to feed the reference modulation. The voltage modulation combining both the reference and the control signals is shown in Figure 6b.

Analytically, based on Equation (28), the turning of the sail can be considered as follows. By definition, $\Omega = \dot{\alpha}$, and it can be seen that

$$\frac{d}{dt}\left(l^3\widetilde{\omega}\cos^2\Lambda\cos\alpha\right) = 0 \tag{29}$$

$$\frac{d}{dt}\left(l^3\widetilde{\omega}\cos\alpha\right) \approx \mathcal{O}(\tan^2\Lambda) \tag{30}$$

as written in terms of the coning angle Λ. Hence, $l^3\widetilde{\omega}\cos^2\Lambda\cos\alpha$ is an adiabatic invariant, and any changes of the sail primary variables $\widetilde{\omega}$ and Λ in the sail angle maneuvers can be determined by using (22) and (29). The adiabatic invariant scaled to its initial value, μ is shown in Figure 6c as determined by the tether variables. Using Equations (23) and (30), the time variation of the tether coning angle and angular frequency can be solved following well the actual time evolution (black solid line) as shown by gray dashed lines in Figures 6d and 6e, respectively. Finally, the tether root tension scaled to the tensile strength of aluminum is shown in Figure 6f.

In general, using Equations (22) and (29), the coning angle (Figure 7a) and the angular frequency (Figure 7b) can be solved as functions of the sail angle. As an estimate, the angular frequency depends on the sail angle as

$$\widetilde{\omega} = \widetilde{\omega}_0\left(\frac{\cos\alpha_0}{\cos\alpha}\right) \tag{31}$$

holding well for the relevant sail angles. The result implies that the amount of the initial angular momentum can be reduced by starting the sail rotation with the sail pointing to the Sun and then turning the sail as shown in Figure 5 to a desired inclination with respect to the Sun. In addition to the tether reeling shown in Figure 4, the tether angular frequency can also be altered by changing the tether angle.

B. Example: Maintaining the sail angle on orbit

The sail angle dependence of the sail spin rate has an important implication on the electric sail dynamics when orbiting around the Sun. As the sail spin plane maintains it orientation with respect to the distant stars (Figure 8a), the sail angle is slowly ($\sim 1^\circ$ per day) changing and the sail

is rotating in the SSE coordinate system along the orbit around the Sun. Equivalently, the rotation can be associated with a weak Coriolis force acting on the tether in SSE. However, to produce constant thrust, the sail angle has to be fixed with respect to the Sun direction. This can be done by the modulation of the electric sail force as depicted in Figures 8b and 8c.

In Figure 8b, the tether tip is on the spin plane (dashed line) at (X_{SSE} =Z_{SSE} = 0) pointing downward (Y_{SSE} = l). Since the SSE system is rotating with $\mathbf{\Omega}$ being anti-parallel to the Y_{SSE} axis, the Coriolis force ($\mathbf{F}_C \propto \mathbf{v} \times \mathbf{\Omega}$) is normal to the sail spin plane. However, as the electric sail force is always aligned with the sun-sail line, only the corresponding component of $\mathbf{F}_C$ can be canceled by the sail force modulation ($\mathbf{F}_{\rm ES}$). While such a modulation maintains the sail attitude with respect to the sun-sail line, the resultant force ($\mathbf{F}_{\rm ES}^{\perp}$) has a component in the direction of the tether tip velocity ($\mathbf{v}$). As this is the case also with the upward orientation of the tether (Figure 8b), the spin rate of the sail slowly increases for positive sail angles (orbiting away from the Sun). For a negative sail angle (spiraling towards the Sun), the spin rate is expected to decrease.

Although this effect may well be negligible in the time scale of the sail rotation periods, the accumulated change in the spin rate has to be taken into account for typical mission time scales. Mathematically, the considerations above are included in Equation (28) for coning angles typical for an electric sail. Now, $\Omega = 2\pi$/year corresponding to the slow rotation of the SSE system along the orbit around the sun. Since the sail angle is kept constant ($\dot{\alpha} = 0$), Equation (28) leads to an differential equation for $\widetilde{\omega}\cos^2\Lambda$ that can easily be solved as

$$\begin{aligned} \widetilde{\omega}\cos^2\Lambda &= \widetilde{\omega}_0\cos^2\Lambda_0 e^{\Omega\tan\alpha(t-t_0)}. \\ \widetilde{\omega} &\approx \widetilde{\omega}_0 e^{\Omega\tan\alpha(t-t_0)} + \mathcal{O}(\tan^2\Lambda). \end{aligned} \tag{32}$$

If the sail angle is negative (positive) and the sail is orbiting towards (away from) the Sun, the spin rate decreases (increases). Figure 9 shows the key sail parameters as a function of time for an time interval of 50 days. These are shown for two sail angles of $\pm 45°$. The voltage modulation (Figure 9a) shows vastly different behavior depending on the sign of the sail angle as expected by Figure 2: For the positive (negative) sail angle, the tether coning angle decreases (increases) while the spin rate increases (decreases). It can be concluded that Equation (32) compares well with the numerical results, and the accumulated changes in the spin rate are significant in terms of mission time scales.

V. Conclusions

The results of this paper are based on a simple dynamical model for the electric sail tether, a spherical pendulum rotating under constant solar wind forcing. This model assumes that the tether is straight, i.e., well tightened by the centrifugal force. We derived rules for the electric sail tether dynamics and control in terms of the key tether variables, coning angle and spin rate. The analysis also provided us with an estimation of the voltage (and thus power) overhead to be reserved for tether control. The amount of overhead depends on the coning angle, implying that a slowly spinning sail requires more voltage reserve for its control than a fast spinning sail. The key variables depend mainly on the exerted electric sail force (tether voltage and solar wind dynamic pressure), tether length, and tether angle. Changes in the electric sail force lead to only minor changes in the tether spin rate while changes in the sail configuration (tether length) and orientation (for typical sail angles) have a major effect on the tether spin rate. This is practical since for a given flight configuration and orientation, the sail spin rate differs moderately from the spacecraft spin rate due to the solar wind variations.

In addition, we described an non-trivial effect of the gradually evolving spin rate arising from the sail orbital motion around the Sun and the related Coriolis effect. The tether voltage modulation can be used to cancel the component of the Coriolis force normal to the sail spin plane and thus maintain the electric sail orientation with respect to the sun-direction. However, the remaining component lies in the spin plane, leading to a cumulative decrease or increase of the sail spin rate for negative (inward) and positive (outward) sail angles, respectively. The reason for this effect is that the electric sail force is not normal to the sail spin plane. Our analytical results showed that the magnitude of the effect is such that it has to be taken into account in typical mission scenarios. While it may somewhat complicate electric sail mission design, a possibility arises that the spin-up angular momentum for the sail deployment could be partly obtained by this effect. Furthermore, a clever control algorithm might be able to mitigate or nullify this effect by utilizing the natural small directional variations of the solar wind.

In this paper we did not consider the effects of the natural solar wind variations. It is likely that when these variations are taken into account, the bare electric sail model consisting only of

tethers and their individual potential control is not able to keep the tethers apart from each other and at the wanted tether angle at the same time. This is because each tether has two degrees of freedom (e.g., the tether angle and the phase angle) while the potential adjustment provides only one control parameter. Therefore it may well be that the electric sail design has to be augmented by some mechanism which keeps the tethers apart, such as auxiliary tethers connecting together the main tether tips [7] or small auxiliary propulsive devices (e.g. solar sails) at the tether tips. Even in the presence of such devices, however, it is beneficial if the applied potential control algorithm is such that it keeps the tethers moving approximately in the right way already by itself. Therefore we consider the bare electric sail model as a useful benchmarking arrangement when developing the potential control algorithm.

Acknowledgments

This work was supported by Academy of Finland.

References

[1] Janhunen, P., "Electric sail for spacecraft propulsion," *J. Propul. Power*, 20(4), 763–764, 2004.

[2] Zubrin, R. M., and Andrews, D. G., "Magnetic sails and interplanetary travel," *J. Spacecraft Rockets*, Vol. 28, 197–203, 1991.

[3] Hoyt, R., and Forward, R. L., U.S. Patent No. 6,286,788 B1, 2001.

[4] Janhunen, P., U.S. Patent No. 7,641,151, 2010.

[5] Janhunen, P., and Sandroos, A., "Simulation study of solar wind push on a charged wire: basis of solar wind electric sail propulsion," *Ann. Geophys.*, Vol. 25, 755–767, 2007.

[6] Toivanen, P. K., and Janhunen, P., "Electric sailing under observed solar wind conditions," *Astrophys. Space Sci. Trans.*, Vol. 5, 61–69, 2009.

[7] Janhunen, P., Toivanen, P. K., Polkko, J., Merikallio, S., Salminen, P., Haegström, E., Seppänen, H., Kurppa, r., Ukkonen, J., Kiprich, S., Thornell, G., Kratz, H., Richter, L., Krömer, O., Rosta, R., Noorma, M., Envall, J., Lätt, S., Mengali, G., Quarta, A. A., Koivisto, H., Tarvainen, O., Kalvas, T., Kauppinen, J., Nuottajärvi, A., and Obraztsov, A., "Electric solar wind sail: Towards test missions," *Rev. Sci. Instrum.*, Vol. 81, 111301, 2010.

[8] Janhunen, P., "Increased electric sail thrust through removal of the trapped shielding electrons by orbit chaotisation due to spacecraft body", *Ann. Geophys.*, Vol. 27, 3089–3100, 2009.

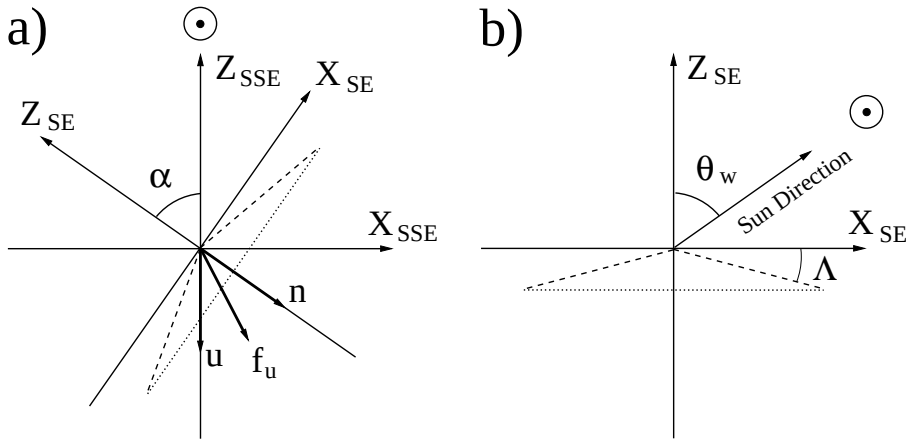

Fig. 1 Coordinate systems of (a) Sail-centric Solar Ecliptic (SSE) and (b) Sail Ecliptic (SE).

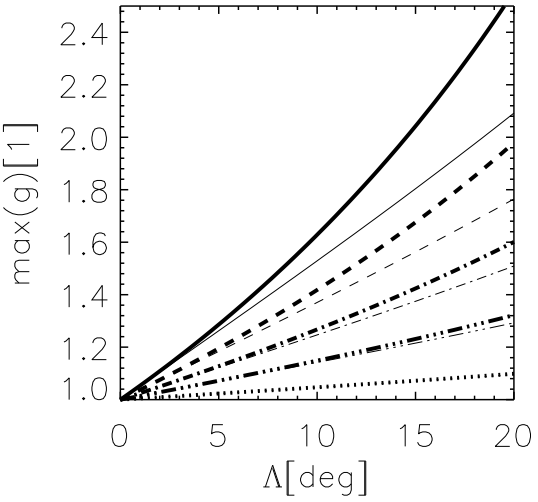

Fig. 2 Maximum of the control reference signal as a function of the coning angle as shown for five sail angles from 5° (thick dotted line) to 45° (thick solid line) with a spacing of 10°. The corresponding thin lines show the approximation for small coning angles.

[9] Sanmartín, J. R., Chroinière, E., Gilchrist, B. E., Ferry, J.-B., and Martínez-Sánchez, M., "Bare-tether sheath and current: comparison of asymptotic theory and kinetic simulations in stationary plasma," *IEEE Trans. Plasma Phys.*, Vol. 36, 2851–2858, 2008.

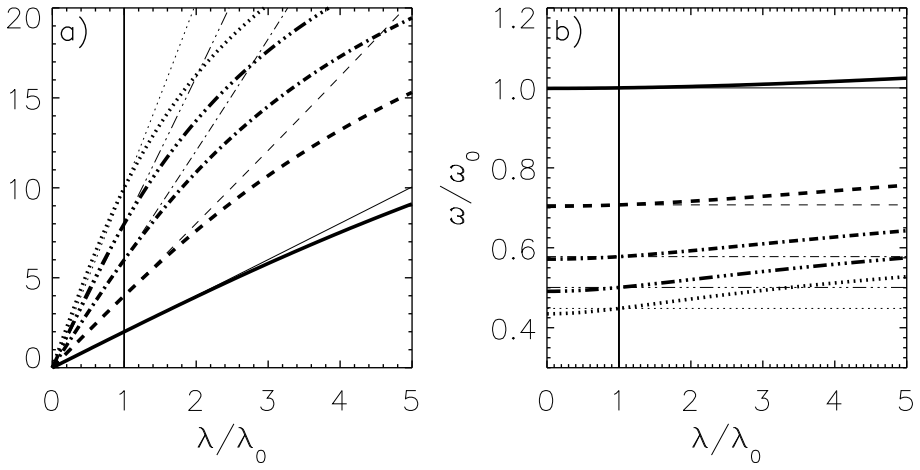

Fig. 3 (a) Coning angle and (b) relative angular frequency as functions of the electric sail force relative to a reference force. Both the adiabatic solution (thick) and its approximate for small coning angles (thin) are shown for five initial coning angles fixed at $\lambda/\lambda_0 = 1$.

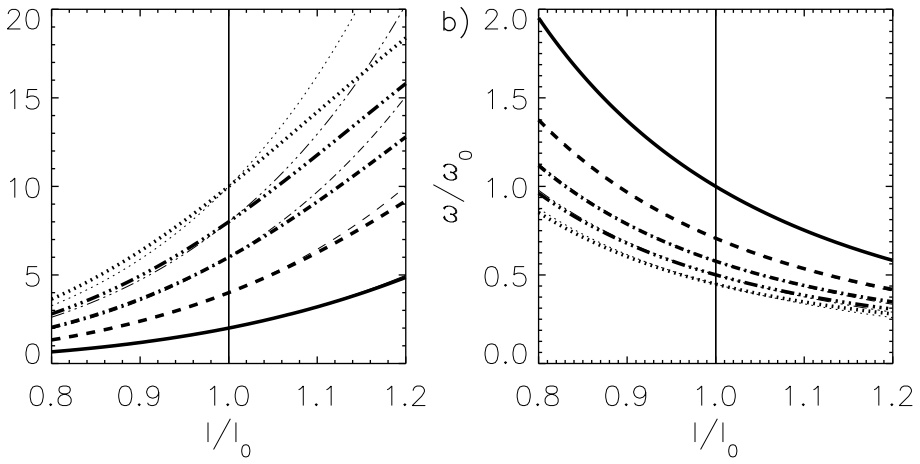

Fig. 4 (a) Coning angle and (b) relative angular frequency as functions of the tether length relative to a reference length. Both the adiabatic solution (thick) and its approximate for small coning angles (thin) are shown for five initial coning angles at $l/l_0 = 1$.

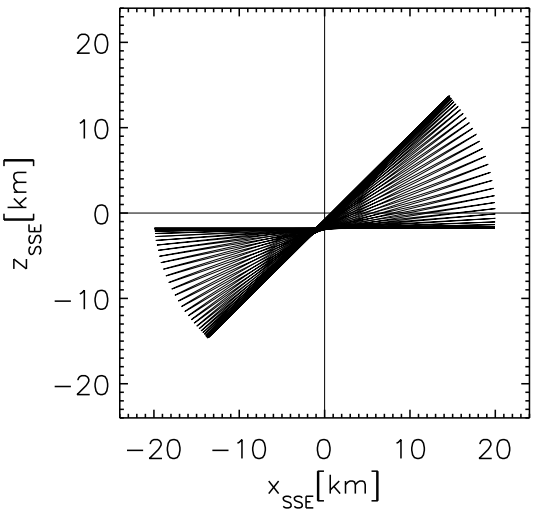

Fig. 5 Trace of the tether tip in SSE coordinates during a turning of the sail from an initial orientation with the sail angle of $\alpha = 0^\circ$ to $\alpha = 45^\circ$.

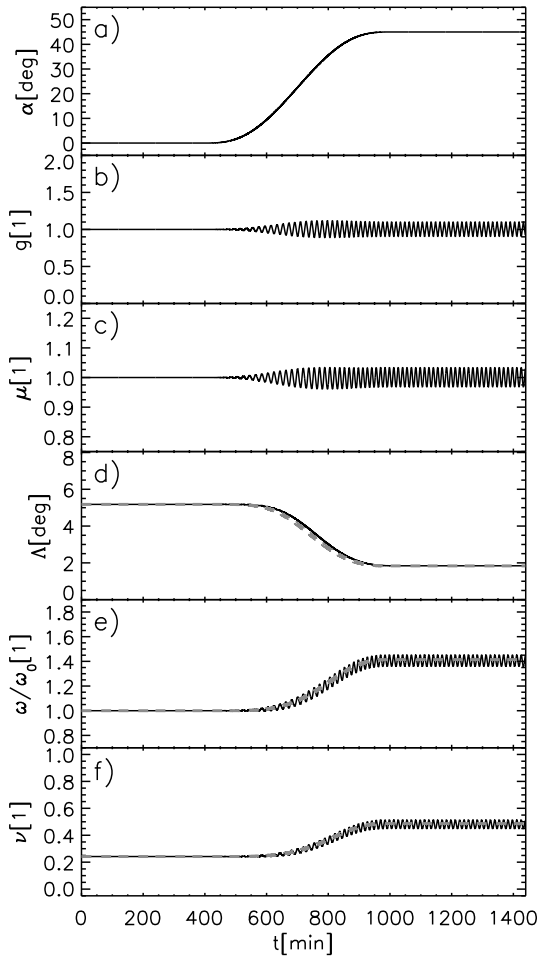

Fig. 6 Temporal evolution of the key sail variables during the sail spin plane turn shown in Figure 5, (a) sail angle, (b) tether modulation signal, (c) relative angular momentum, (d) coning angle, (e) relative angular frequency, and (f) tether root tension. The gray dashed curves show the result of the adiabatic approximation.

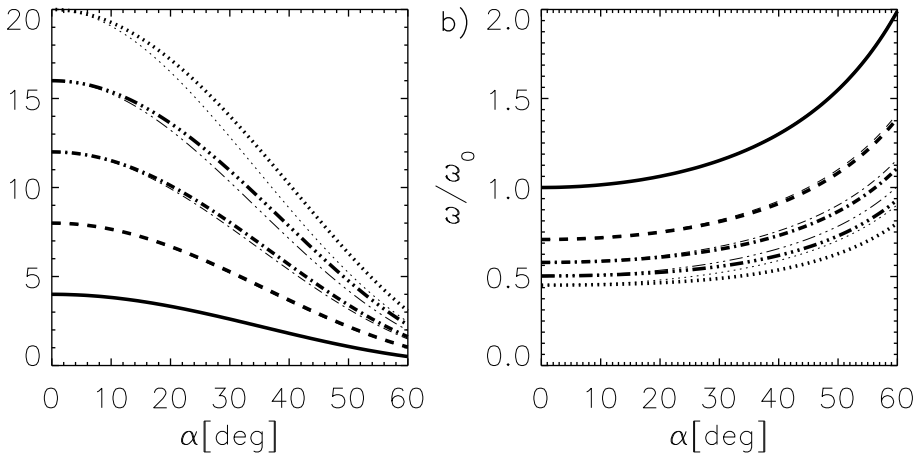

Fig. 7 (a) Coning angle and (b) relative angular frequency as a function of the sail angle. Both the adiabatic solution (thick) and its approximate for small coning angles (thin) are shown for five initial coning angles fixed at $\alpha = 0$.

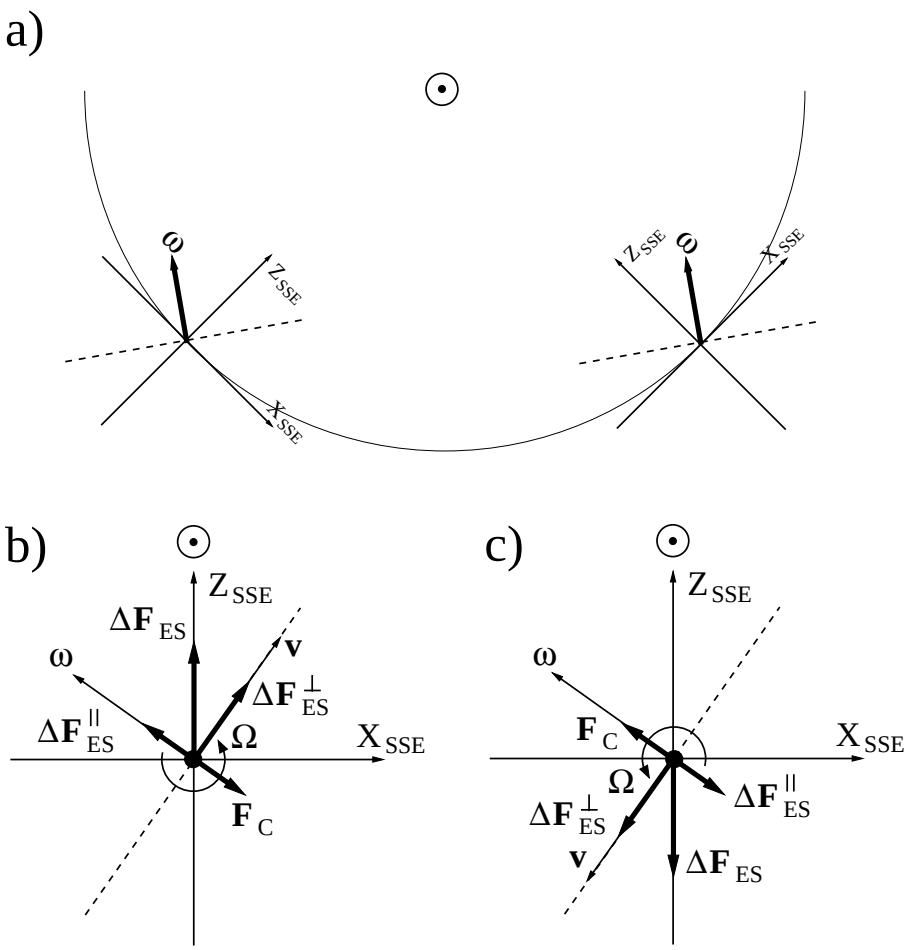

Fig. 8 (a) Sail spin plane (dashed line) orientation with respect to the distant stars and to the SSE system while orbiting around the Sun with no spin plane control applied. Orientations of the Coriolis force ($\mathbf{F}_C \propto -\boldsymbol{\Omega} \times \mathbf{v}$) acting on the tether pointing (b) anti-parallel and (c) parallel to the $\mathrm{Y_{SSE}}$ axis. The sail spin plane can be fixed with respect to the sun direction (positive sail angle shown) by modulation of the electric sail force ($\Delta\mathbf{F}_{\mathrm{ES}}$) that cancels the Coriolis force ($\mathbf{F}_C$) aligned with the sail spin axis. However, the resultant force ($\Delta\mathbf{F}_{\mathrm{ES}}^{\perp}$) is in the direction of the tether velocity (v) leading to a gradual increase in the tether spin rate in the case of the positive sail angle (the sail is orbiting outward). For a negative sail angle (orbiting inward), the spin rate is decreased (not shown).

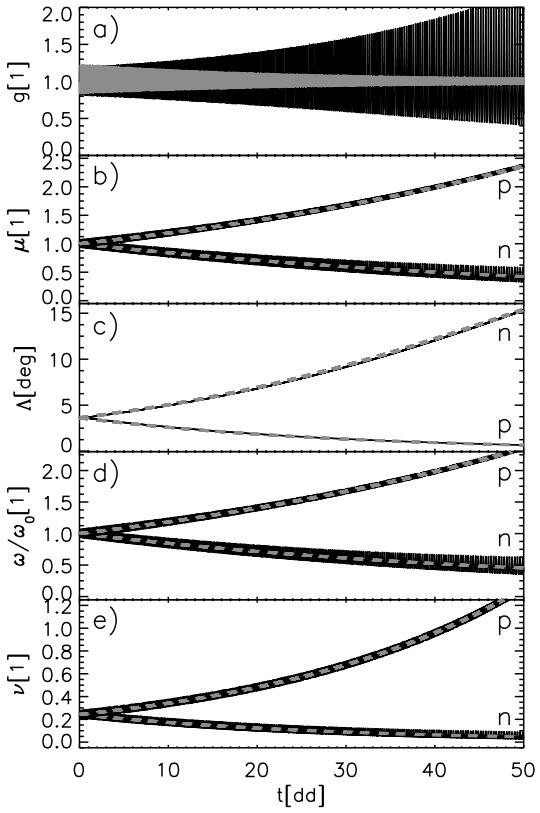

Fig. 9 Temporal evolution of the key sail variables during 50 days while orbiting around the Sun as shown for both the positive and negative sail angles: (a) Tether voltage modulation for positive (black) and negative (gray) sail angles, (b) relative angular momentum, (c) coning angle, (d) relative angular frequency, and (e) tether root tension. The black lines show the result of the numerical computations, and the dashed gray lines show the result of the analytical calculations for the positive (p) and negative (n) sail angles.